IEEE Access
Multidisciplinary | Rapid Review | Open Access Journal

Received March 16, 2020, accepted March 21, 2020, date of publication March 24, 2020, date of current version April 8, 2020.

Digital Object Identifier 10.1109/ACCESS.2020.2983115

Model Predictive Control for Indirect Boost Matrix Converter Based on Virtual Synchronous Generator

JONGGRIST JONGUDOMKARN[1], JIA LIU[1], (Member, IEEE), YUTA YANAGISAWA[1], (Student Member, IEEE), HASSAN BEVRANI[2], (Senior Member, IEEE), AND TOSHIFUMI ISE[3], (Member, IEEE)

[1]Division of Electrical, Electronic, and Information Engineering, Osaka University, Osaka 565-0871, Japan
[2]Smart/Micro Grids Research Center, Department of Electrical Engineering, University of Kurdistan, Sanandaj 66177-15175, Iran
[3]Nara–Gakuen Incorporated Educational Institution, Nara 636-8503, Japan

Corresponding author: Jia Liu (liu@pe.eei.eng.osaka-u.ac.jp)

ABSTRACT Indirect boost matrix converter is potentially a great alternative to a back-to-back converter for permanent magnet synchronous generators based distributed generation since it can achieve a voltage-boost functionality without utilizing a bulky DC-link capacitor. Despite the success of the indirect boost matrix converter topology, there still exist some issues in the relevant control structure that must be resolved appropriately. First, the existing controls are grid-following controls, which is incapable of islanded operation. Secondly, the exiting controls generate a highly distorted current waveform, which needs to be suppressed by a passive damping resistor. Moreover, without an energy storage element, the distributed generations have no short-time power reserve unit for providing an inertial power to support the utility. In order to solve these issues, a novel approach based on a modified virtual synchronous control and a finite control set model predictive control scheme is proposed in this paper. The former is adopted to ensure proper operations in both grid-connected and islanded modes and to emulate the virtual inertial response by drawing inertial power from the input source. The latter utilizes multi-controls of real-time variables to avoid complicated coupling between the input side and the output side controls and to grant the indirect boost matrix converter with the capability of providing active filter resonance damping. Comparative studies between the proposed control and its existing counterpart are conducted with several simulations in PSCAD/EMTDC software to demonstrate the superior performances of the proposed strategy. Finally, the proposed control is verified in a scale-down experiment testbed.

INDEX TERMS AC-AC converters, distributed power generations, indirect matrix converter, power control, power system stability, predictive control, virtual synchronous generator.

I. INTRODUCTION

AC/AC converter can broadly be found in standard industrial applications such as adjustable speed motor drives and power quality conditioners. Among them, the applications in distributed generation (DG) with variable ac-source using a permanent magnet synchronous generators (PMSGs), such as wind turbines, hydrokinetic turbines, and gas engine, have recently attracted a lot of attention from power engineers. Currently, the conventional back-to-back (B2B) converter [1]–[3] is a preferred choice for interfacing decentralized sources and the utility distribution grid. However, bulky and limited-lifetime DC-link electrolytic capacitors are still often considered as the disadvantages of B2B converters. Hence, matrix converters (MCs) [4]–[17] are commonly investigated as a possible alternative for B2B converter since only a small or no dc-link capacitor is involved in the MCs topology. This is especially beneficial for applications where volume and weight restrictions are required. Nevertheless, the downside of MCs is that any change in the power command must be compensated by the energy stored in the DG unit itself, unlike in the case of the B2B converter,

The associate editor coordinating the review of this manuscript and approving it for publication was Lei Chen.

where the dc-link capacitor provides short-time energy and decouples the rectifier and inverter stages. Therefore, the control schemes for MC are more complex.

The MCs can be typically categorized into two types [4]: conventional direct matrix converters (DMCs) and indirect matrix converters (IMCs). Conventionally for a three-phase to three-phase conversion, a direct matrix converter utilizes nine bidirectional transistor-switches to establish a direct connection between the input and the output. Such an arrangement provides full bidirectional power flow, which is not useful for DGs, where power is only flowing from the sources to the distribution grid and thus causing a surplus of transistor switches [18]. The IMCs, on the other hand, can be simplified to reduce the number of transistor switches if a unidirectional power flow control is utilized. An IMC is composed of a voltage source converter and a current source converter. This topology is also known as sparse matrix converters (SMCs) [11]–[13]. Nevertheless, both SMCs and general DMCs have a low voltage gain, which is a limiting factor for a grid interfaced with DGs. This is notably the case for a connection between the utility and variable source voltages such as a PMSG-based energy conversion system driven by a wind turbine or gas engine, as these variable sources operate in a variable speed mode, during which a varying voltage ranged from a low voltage to the PMSG rated voltage is generated. Therefore, a number of methods to increase the voltage gain have been proposed in the literature. The strategy can be done either in the modification of modulation strategies, as suggested in [14], or in the modification of the topology by adding more components to the virtual dc-link, as presented in [15]–[16]. Nevertheless, these methods can cause other disadvantages to the system. For instance, high filter requirements are needed for the given method in [14] due to higher input current total harmonic distortion (THD), and the adding of passive components will increase overall system losses.

Alternatively, references [17] and [18] proposed an implementation of a reverse power flow operation of IMCs to generate a voltage-boost property. This configuration is an attractive solution for DG applications as it achieves a voltage gain larger than 1.4 just by reversing the order of the IMC to have a current source converter at the grid side and a voltage source converter at the side of the power source. It will be termed as an indirect boost matrix converter (IBMC) in this paper. Although the advantages of IBMC topology are clearly noticeable, the existing control methods are almost directly adopted from IMCs with conventional topology. Therefore, some shortcomings still exist, for instance, the resonance phenomenon of output *CL*-filter caused by the generation of low order harmonics components. This resonance may profoundly disturb the output current [8], so that it usually requires the addition of a passive damping resistor at the grid interfacing side [17], [18]. The existing modulation methods also only utilize the information of the phase angle to control the CSI side, and the amplitudes of output values cannot be regulated directly due to the fact that zero current vectors are not be used in the CSI side of IBMC [17], [18]. Thus it is challenging to apply active damping with such a control method. Another shortcoming of the existing control method lies in the fact that the existing control schemes are grid-following controls, which are only capable of operation in the grid-connected mode. Although a control scheme for islanded operation is proposed in [18], it faces a challenge of managing the transition of control mode between grid-connected and islanded operation. Furthermore, grid-following controls do not actively control their output frequency to support grid frequency stability. This is an essential topic for the future grid, where DGs are highly penetrated because, unlike synchronous generators (SGs), DGs lack rotating inertia.

One of the highly-rated solutions for these problems is the implementation of a virtual synchronous generator (VSG). The results of the past research works have clearly demonstrated that the VSG-based DGs can solve issues related to frequency deviations, and also capable of islanded operation [19]–[27]. However, the referred VSG controls are typically designed for a system with energy storage elements such as the B2B converter-interfaced system, as the inertial power of the referred VSG controls is provided by this storage element. Therefore, it is challenging to implement these VSG controls in a system without a dc-link energy storage element, such as the IBMC-interfaced DG. Without the energy storage element to draw a short-time power from, the controller needs to be able to dispatch the power directly from the input source in order to support the frequency stability of the grid. Furthermore, the integration of VSG control will further complicate the modulation of IBMC, which is already complicated due to the coupling between input control and output control.

Over the last few years, finite control set model predictive control (FCS-MPC) has emerged as an attractive alternative for the control of power electronics applications since it offers several benefits including simple multivariable control, the possible inclusion of constraints, straightforward control law, and fast dynamic response [30]. As for DGs, a number of control solutions based on FCS-MPC appeared in the literature [31]–[36]. Among these, the multivariable FCS-MPC-based VSG for a voltage source inverter (VSI) proposed in [36] shows high compatibility between the FCS-MPC and VSG. In addition to an integration of the inertia support feature, the FCS-MPC-based control scheme utilizes a simultaneous control of both voltage and current of the output *LCL*-filter, to provide a fault-ride-though ability, and to restrain the resonant energy oscillation between the inductances and the capacitances. The mentioned oscillation will occur if either one of the filter voltage or the filter current is solely controlled. This performs an alternative method to damp the filter resonance without a dedicated active damping part in the control algorithm [36]–[39].

The FCS-MPC constitutes a promising approach for implementation of VSG control-based IBMC compared with standard schemes because the FCS-MPC allows several

control objectives to be fulfilled simultaneously by utilizing the system model and the real-time values of the system to determine the optimized converter's physical switching states directly. This grants the predictive controller significant advantages over the existing PWM-based methods, as it is capable of regulating the amplitudes of output values without employing zero current vectors. Therefore, the FCS-MPC is more suitable for the implementation of VSG controls, which govern the reactive output power via the regulation of output voltage amplitude. Furthermore, with the real-time variables of physical dc-link used in system model prediction, considerations of the complicated coupling between rectifier and inverter to find the mean values of the dc-link variables can be removed from the control algorithm as shown in the studies of FCS-MPCs for conventional motor/load drive IMC [40]–[42]. Taking into account the investigated flaws of the existing method, such as the usage of a grid-following strategy and the requirement of a passive damping circuit, a novel VSG control based on the FCS-MPC is proposed to improve the performance of the IBMC-based DG. First, thanks to the adoption of the VSG strategy, the ability to operate in both grid-connected and islanded modes is achieved, while the controller is capable of dispatching the inertial power directly from the input sources, and is able to regulate the output reactive power through the manipulation of the output voltage. Furthermore, active filter resonance damping is provided by the multivariable control of capacitor voltage and inductor current of the output *CL*-filter.

The rest of this paper is organized as follows. In Section II, the topology of IBMC and the relevant existing control methods are discussed. The shortcomings of the control method under investigation are analyzed and verified with simulation results shown in this section. The novel VSG control for IBMC based on FCS-MPC is proposed in Section III. In Section IV, the performance of the proposed control scheme is verified by simulation results along with discussions to highlight its advantages. Experimental verification is then conducted in a scale-down manner in Section V to validate the results of the simulation study. Finally, this paper is concluded in Section VI.

II. IBMC CONVERTER: A REVIEW

A. TOPOLOGY

A topology of unidirectional IBMC is illustrated in Fig. 1. The converter consists of twelve power transistor switches. Among these, six switches have antiparallel diodes and are arranged as a front-end voltage source rectifier (VSR). The other six switches have series diodes for forming a rear-end current source inverter (CSI). This topology clearly differs from conventional IMC, where current source rectifier (CSR) and VSI are utilized. This reversed configuration allows the IBMC to have boost property. Nevertheless, according to [18], a clamped diode in series with a small film capacitor termed as "fictitious dc-link" is required at the physical link between VSR and CSI as a mean to maintain dc-voltage and suppress its spike.

This dc-link capacitor is vital for IBMCs because VSR utilizes zero voltage vectors, during which all the upper or lower switches of the VSR are turned on, and the dc-link current becomes zero. As a consequence, no dc current is supplied to the CSI, and thus all switches in the CSI are turned off. Without the DC-link capacitor, this will result in DC-link voltage becoming zero, which should be avoided as it can cause short-circuits between output filter capacitors and antiparallel diodes in the VSR side. However, the presence of the DC-link capacitor means that DC-link voltage can be discharged via the CSI to the output filter capacitances, generating a sizeable circulating current and distorting the output current of the IBMC. In order to avoid this, the DC-link capacitor should be so small that the amount of the discharging current is ignorable. However, the voltage spikes will not be sufficiently suppressed in this case. Alternatively, as shown in Fig. 1, a clamping diode could be added in series with the capacitor to prevent the discharging, thus allowing a larger DC-link capacitor to be used.

B. EXISTING PWM-BASED MODULATION METHOD FOR IBMC

The investigated modulation methods of CSI and VSR in this section are adopted from [17], [18]. as mentioned previously,

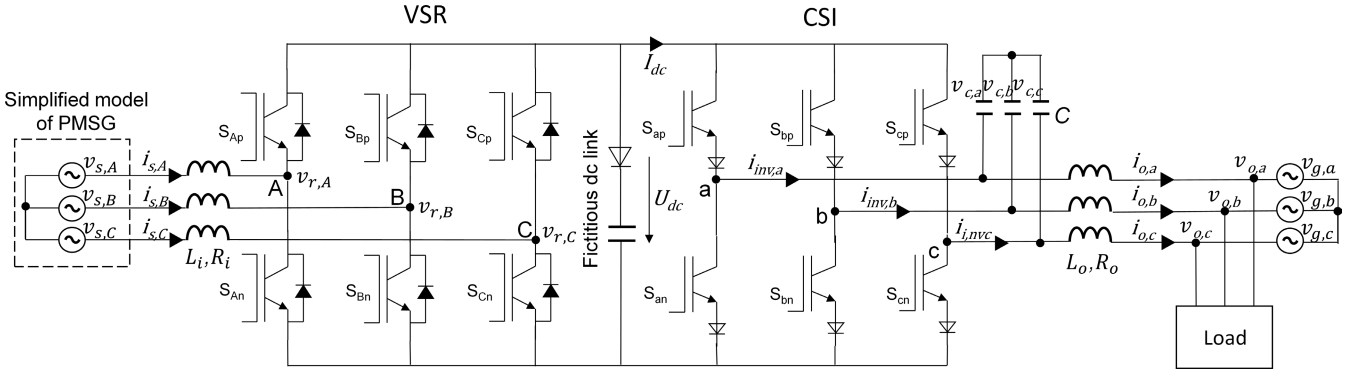

FIGURE 1. Topology of indirect boost matrix converter.

the controllers of the CSI and VSR have to be dependently implemented since there is no dC-link capacitor to decouple the two stages. Here, the modulation of each stage is briefly explained.

1) CSI SIDE

The objective of modulation in the CSI side is to keep the dc-link voltage commutating between the largest and the second-largest positive line-to-line grid voltages. In this method, none of the null states are used to avoid circulating current between the fictitious dc link and the shorted phase-leg. The reference IMC output current can be synthesized by making use of the two adjacent active current vectors from the possible six active vectors (SC1-SC6), which divide the space vector into six sextants, as illustrated in Fig. 2. The reference current phasor is set to follow grid phasor, thus, if the grid phasor θ_g is located in one of the sextants, two nearest space vector to the reference current phasor will be chosen. The zero current vectors are not used in CSI to avoid a short-circuit at the DC-link capacitor. Nevertheless, if we consider Fig. 2, it can be seen that when the IMC output current is generated only from two active current vectors, the amplitude of the current cannot be adjusted due to the absence of zero current vectors. Under this condition, only the synthesized current vectors on the hexagon boundary that is depicted in Fig. 2(a) can be generated. Therefore, the corresponding active duty ratios (d_1 and d_2) used for gating the modulated transistor switches within a sampling period of the CSI can be determined with the three-phase angles θ_a, θ_b and θ_c alone, giving the fact that $cos\theta_a + \cos\theta_b + \cos\theta_c = 0$. For the example of sextant 1, the ratio d_1 that the first modulated switch (S_{bn}) is turned on and the ratio d_2 that the second modulated switch (S_{cn}) is turned on can be eventually determined as follows:

$$d_1 = -\cos\theta_b/\cos\theta_a, \quad d_2 = -\cos\theta_c/\cos\theta_a \tag{1}$$

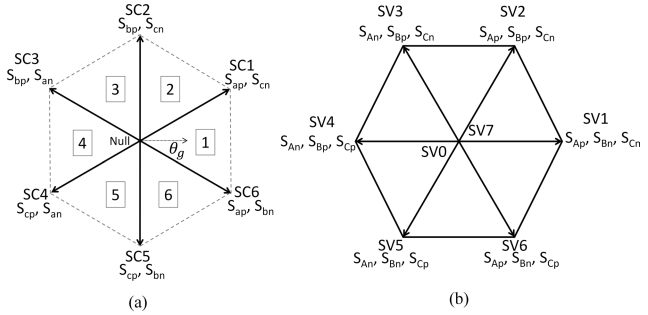

FIGURE 2. Space vector representation of (a) CSI, and (b) VSR.

Since the amplitude of the current cannot be adjusted through modulation in the CSI side, in order to create a sinusoidal current, the modulation method is instead designed to manipulate the dc-link current through modulation in VSR. This can be achieved by applying the following average dc-link voltage (2) during the calculation of the VSR side's modulation index.

$$V_{DC(av)} = \begin{cases} \dfrac{3V_{om}}{2\,|m_{max}|} cos\emptyset_0, & \text{for sextants} = 1, 3, 5 \\ \dfrac{3V_{om}}{2\,|m_{min}|} cos\emptyset_0, & \text{for sextants} = 2, 4, 6 \end{cases} \tag{2}$$

where $m_{max} = max(\cos\theta_a, \cos\theta_b, \cos\theta_c)$, $m_{min} = min(\cos\theta_a, \cos\theta_b, \cos\theta_c)$, and $\emptyset_0$ is the output power factor angle. Because of (2), the resulting average amplitude of dc-link current ($i_{DC(av)}$) would vary in inverse proportion to $v_{DC(av)}$.

2) VSR SIDE

For the control of the VSR side, the space vector modulation (SVM) is implemented to produce the desired input current. The VSR switching sequence must utilize zero space voltage vectors (SV0 and SV7) shown in Fig. 2(b) to boost the input voltage (i.e., using the input inductance). The reference voltage vectoris synthesized by making use of the zero voltage vectors and two adjacent active vectors of the possible six active vectors (SV1 – SV6).Additionally, compensation for the varying dc-link voltage (2) has to be executed. Hence, the modulating reference d_A for phase A can be written with the following equation.

$$d_A = \frac{v_A + V_{off}}{V_{DC(av)}/2} \tag{3}$$

where v_A, v_B and v_C represent three-phase input voltage references without normalization. V_{off} is the triple order harmonic offset commonly added to gain a 15% increase in the modulation index [9]. Finally, coordination between the commutation of CSI and VSR modulations is required to avoid an error. This can be done via an arrangement of the modulation periods of both VSR and CSI side controls. More relevant explanations can be found in [10], [18].

C. ANALYSIS OF CONTROL ALGORITHM FOR DG APPLICATIONS

Despite the effort to compensate dc-link current through modulation in VSR, the modulation alone cannot correctly generate the desired dc-current amplitude, and low harmonic order components are generated in the CSI side. These harmonics seem to be amplified in the control of IBMC since the IBMC is connected to voltage sources in both input and output sides as opposed to conventional RL-load drive IMC, where voltage source only exists at the input side. The differences in frequencies, phase angles, or amplitudes between input and output voltage sources are bound to affect the generated dc-link current. Hence, low order harmonic distortion can be observed in the generated output current waveforms. This low harmonic order may excite *CL*- filter resonance in the grid side of IBMC, which causes the output current to be highly distorted, as shown in [8]. In order to suppress the oscillation caused by filter resonance, it requires the addition of a passive damping resistor at the grid interfacing side, as suggested in [17], [18]. Nevertheless, it will cause high power losses

in the converter. Although various active damping strategies to eliminate distorted input current of RL-drive IMC are proposed in the literature [28]–[29], which could possibly be modified for the suppression of distorted output current of IBMC, they require a complex modification in control algorithm and higher switching frequency, which causes higher switching losses. Hence, similarly to [17], [18], a damping resistor is added to the circuit, as shown in Fig. 3 to deal with resonance issues in this work.

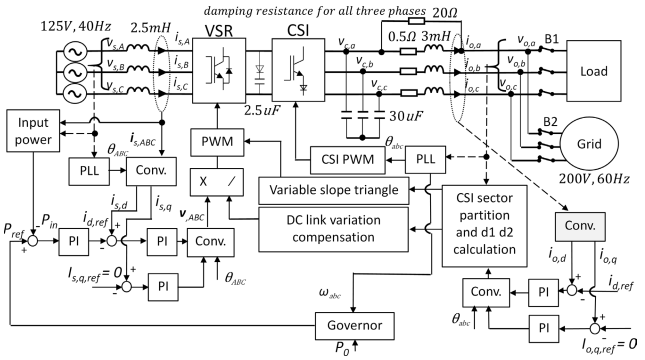

FIGURE 3. The control diagram of the existing PWM-based method.

The objective of DGs in grid-connected operation is to track the dispatch power command, which is realized by the control diagram shown in Fig. 3. The current command $i_{d,ref}$ of VSR is obtained via PI control of the outer active power control loop. The active power command is set at 5 kW. For unity power factor operation, $i_{s,q,ref}$ is set to zero. The computed current reference is subsequently tracked by the measured source current $\boldsymbol{i}_{s,dq}$ by feeding their error to a PI controller. As for the CSI, three-phase modulation references are obtained through *dq/abc* transformation after the PI control processing, as shown in Fig.3. The same current command $i_{d,ref}$ as used in the VSR side is employed and for unity power factor operation, $i_{o,q,ref}$ is set to zero. However, only the phase angle information is used for the CSI modulation, as shown in (1). The other block diagrams, shown in Fig. 3, are well described in [17], [18].

The modulation index of the CSI is fixed at 1 since only the phase angle information is used. This arrangement is suitable for IMC without reversed configuration, where modulation of CSR is set to the maximum so that the power can be designed by the VSI side's control and the load. The output power of the IBMC, on the other hand, is managed by the input control and is not affected by the output network. This implies that the control algorithm for the IBMC is not suitable for islanded operation, where the balance between DG's power and load power needs to be maintained. A different control scheme is suggested in [18] for the islanded operation of the IBMC, which utilizes the measured output voltage drop in order to determine the power command for the VSR controller according to the relationship of $P = V^2/R$. However, this method requires control modes changing between grid-connected and islanded operations. Furthermore, the relationship between output voltage drop and output power can only be accurately deployed if no reactive load exists in the islanded network.

In order to study the performance of the existing PWM-based method for IBMC, the test circuit depicted in Fig. 3 is used for simulations in PSCAD/EMTDC. The DG system is connected to the grid and is set to operate according to the droop characteristic with the reference active power obtained following the equation of $P_{ref} = P_0 - k_p(\omega_{abc} - \omega_{base})$, where ω_{abc} is the measured grid frequency, ω_{base} is grid nominal frequency, which is fixed at 376.99 rad/s and the frequency droop gain k_p is chosen at 40 pu for which nominal output power P_0 is set at 5 kW. The effect of filter resonance is first simulated by removing the resistive damping. The PI parameters of the current control loops ($k_{p,i}$ and $T_{i,i}$) are selected as 0.5 pu and 0.0025 pu, respectively. Sampling frequency $f_{s,csi,pwm}$ 10 kHz is selected for the CSI of the PWM-based method, which results in the average switching frequency of 20 kHz and 10 kHz for the VSR and the CSI, respectively.

The dc-link voltage, the input current, the dc-link current, and the output current for the case without the damping resistor are illustrated in Fig. 4. It can be seen that without damping resistor, significant distortion (due to filter resonance) appears in output current waveform. The input power injected to the converter amounts to 5 kW. The input and output reactive powers are maintained at 0 var to obtain unity power factor.

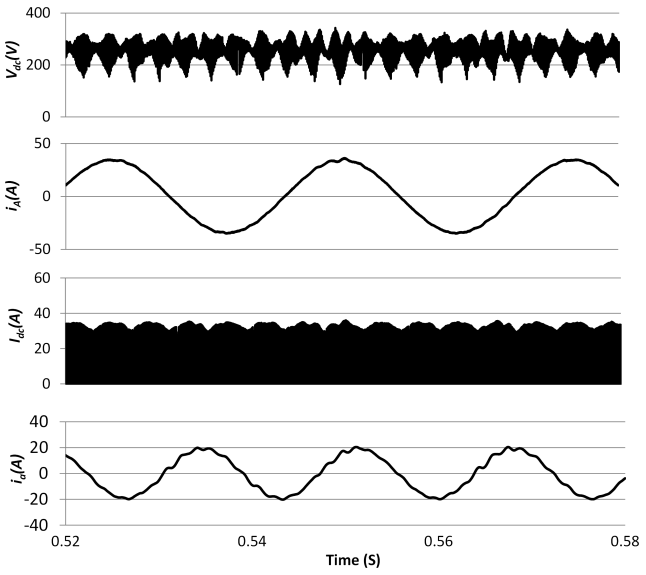

FIGURE 4. Simulation results of steady-state waveforms of tThe dc-link voltage, the phase-A input current, the dc-link current, and the phase-a output current of the PWM-based method without damping resistor, from top to bottom, respectively.

To suppress the filter resonance, a damping resistor R_d is required in the circuit, as previously discussed in this subsection. According to [17], the transfer function of output current i_o with respect to inverter current i_{inv} and grid voltage v_g when R_d is added in parallel with the output filter can be

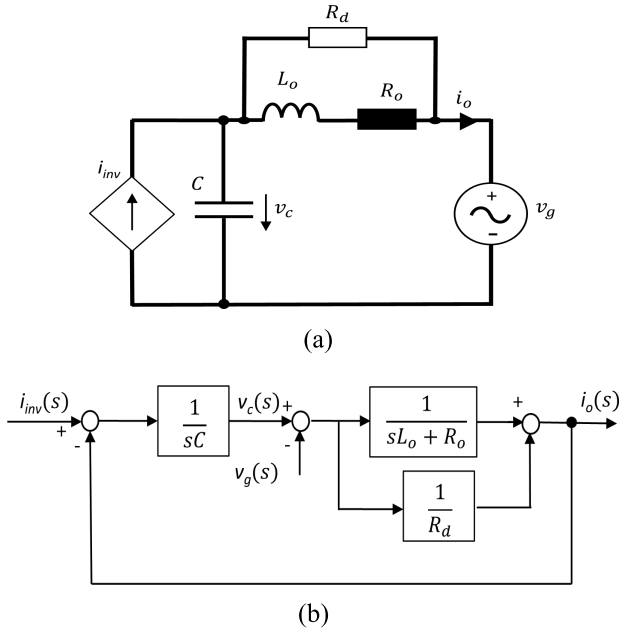

FIGURE 5. Model and block diagram for phase-a current in CSI side of the IBMC: (a) Model; (b) Block diagram.

derived based on Fig. 5 as follows.

$$\boldsymbol{i_o} = \frac{sL_o/R_d + 1}{s^2L_oC + s\left(R_oC + L_o/R_d\right) + 1}\boldsymbol{i_{inv}} - \frac{\frac{s^2L_oC}{R_d} + sC}{s^2L_oC + s\left(R_oC + \frac{L_o}{R_d}\right) + 1}\boldsymbol{v_g}, \quad (4)$$

where R_o, L_o and C are defined as shown in Fig. 1. Derived from (4), the damping ratio ζ for the second-order system can be calculated with (5).

$$\zeta = \frac{R_oC + L_o/R_d}{2\sqrt{L_oC}} \quad (5)$$

According to (5), the presence of R_d can increase the ζ. Hence, R_d equal to 20 Ω is added to achieve the desired damping. The dc-link voltage, the input current, the dc-link current, and the output current for this case are illustrated in Fig. 6. As can be seen in the figure, distortion in output current is significantly eliminated. However, the losses in the output filter resistances increase because of the damping resistor. The total losses are approximately 300 W, which amounts to around 6 % of the input power. We can conclude from this result that the using of passive damping is not an attractive solution for the filter resonance suppressing due to the losses inflicted by R_d. The THDs of input and output currents of the converter during steady-state are concluded in Table 1.

Although a droop controller is applied, this method is still a grid-following control. Thus, it is not capable of operating when the converter is disconnected from the grid. To validate this, the test circuit is simulated for the case of sudden islanding from the grid at time $T = 1$ s. The output power and the output frequency illustrated in Fig. 7 clearly show that the controller has no mean to control the output frequency, as it

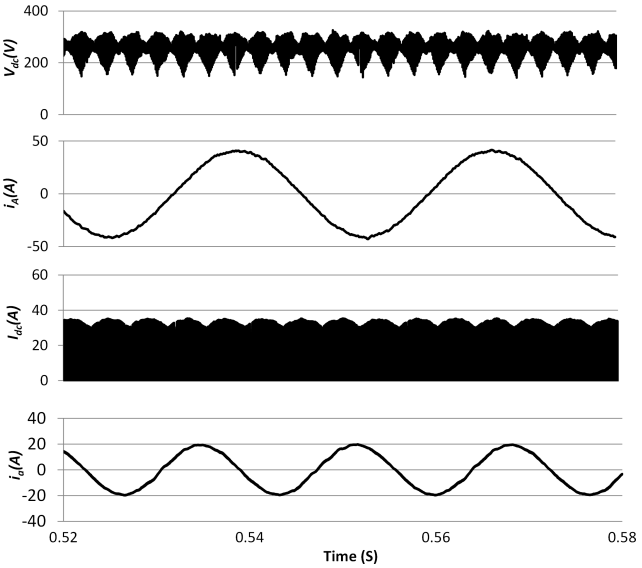

FIGURE 6. Simulation results of steady-state waveforms of The the dc-link voltage, the phase-A input current, the dc-link current, and the phase-a output current of the PWM-based method with a damping resistor, from top to bottom, respectively.

TABLE 1. Current THDs for existing PWM-based method.

Condition	Output current *THD*	Input current *THD*
The PWM-based method without damping resistor	≈ 7 %	≈ 3 %
The PWM-based method with a passive damping resistor	≈ 3 %	≈ 2 %

keeps rising after grid islanding. The increase in frequency also leads to a decrease in output power due to the characteristic of the *Pf*-droop controller since the output power of the IBMC is determined purely by the power command of VSR and is not affected by the output network. The power command decreased until it reached zero, and the control system collapsed, as illustrated in Fig. 7. This figure also indicates that the controller cannot maintain the amplitude of the output voltage when the DG is islanded from the grid due to the nature of the modulation methods for the IBMC, which only utilizes the phase information in the control of the inverter side and has no control over the amplitude of the output voltage. All of these emphasize the unsuitability of such modulation methods for the implementation of the grid-forming-based VSG control, which needs to be able to control both voltage and frequency actively.

III. THE PROPOSED MPC-VSG BASED CONTROL SCHEME

The IBMC topology used for the proposed control scheme is adopted from the one explained in section II. It consists of a VSR and a CSI, as shown in Fig. 1. However, the topology for the proposed scheme differs from the one in Fig. 1, since the clamp diode is removed from fictitious dc-link, as shown in Fig. 8. Because in the proposed control scheme, distortion in capacitor voltage caused by discharging current from the dc-link capacitor, as happened in the PWM-based method

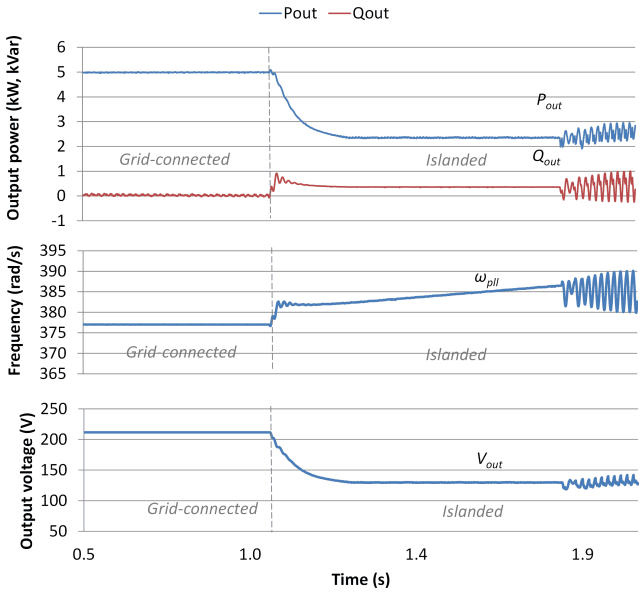

FIGURE 7. Simulation results of tThe output active and reactive power, the output frequency and the output voltage amplitude of the existing PWM-based method with a damping resistor before and after grid-islanding, from top to bottom, respectively.

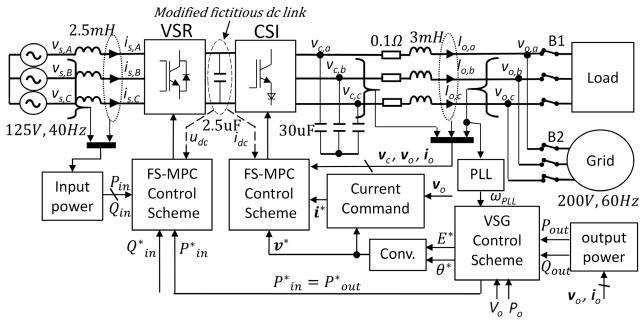

FIGURE 8. The proposed control diagram of the FCS-MPC for IBMC-based VSG.

when a clamp diode is absent, can be avoided with direct control of capacitor voltage. Furthermore, the short circuit in parallel diodes of the VSR side under a negative dc-link voltage can be prevented by including an additional constraint in the cost function, as explained in section III-B.

The overall control diagram of the proposed control is shown in Fig. 8. It is composed of the FCS-MPC and VSG control parts. The FCS-MPC part predicts the system variables and evaluates the optimal switching states for both VSR and CSI sides. In the VSG control part, the command variables of both sides of the converter, such as output voltage command, output current command, and input power command, are determined. The former part will be explained in Part-B, whereas the latter part is discussed in Part-C.

A. THE PROPOSED VSG CONTROL FOR THE IBMC

1) VSG CONTROL

The objective of VSG is to track the dispatch power command while providing virtual inertia to the DG to slow down any deviation of the grid frequency. This can be realized with

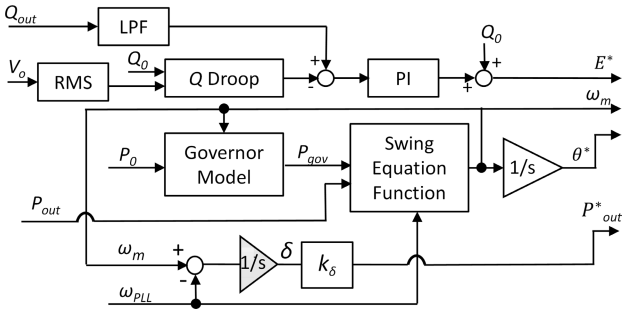

FIGURE 9. The control diagram of the proposed VSG control scheme.

the structure of a DG using VSG control shown in Fig. 9. It consists of "Swing Equation Function", "Governor", and "Q droop" parts. P_o, P_{out}, P_{gov}, Q_o, Q_{out}, V_{out}, ω_m, ω_{PLL}, E^* and θ^* represent the output active power command, the output active power, the shaft power from governor, the output reactive power command, the output reactive power, the output voltage amplitude, the mechanical frequency of rotors, the output frequency measured by PLL, the voltage reference magnitude, and the power angle reference, respectively. Virtual inertia is emulated in the block "Swing Equation Function" with the help of the well-known swing equation (6).

$$P_{gov} - P_{out} + D(\omega_m - \omega_g) = J\omega_m \frac{\mathrm{d}\omega_m}{\mathrm{d}t} \tag{6}$$

where J is the moment of inertia, D is the damping factor produced by the damper windings, P_{out} is the output active power, ω_m is the virtual rotor angular frequency, and ω_g is the grid frequency. The function of the shaft power P_{gov} regulated by a governor is shown in (7).

$$P_{gov} = P_0 - k_p(\omega_m - \omega_{base}) \tag{7}$$

where k_p is the droop coefficient and ω_{base} is the nominal grid frequency. The block "Q droop", as well as the design details of all blocks in Fig. 10, and the tuning of VSG parameters, are all explained in [27] and hence will be omitted in this work.

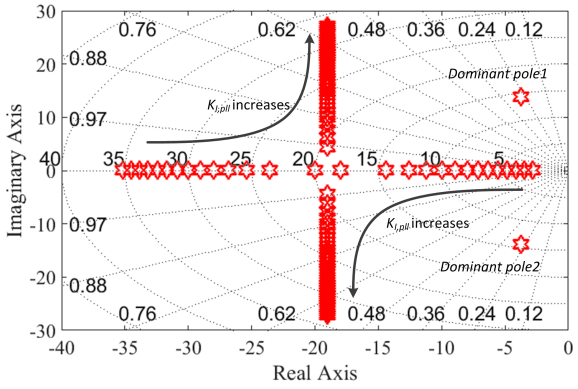

FIGURE 10. Eigenvalue loci with changing of $k_{i,pll}$.

In the previous research works of VSG applications for the VSIs [26], [27], [36], the output active power of the converter

was drawn directly from the energy storage element in correspondence to the phase angle difference between the inverter output voltage and the grid voltage. Hence, the output power of such VSG control can be regulated by merely controlling the output voltage. However, due to the lack of energy storage elements in the present work, the output power of the IBMC must be controlled by the input power command of the VSR side, as the output power will follow the controlled power flows from the VSR to the fictitious dc-link before reaching the output network. Thus, the output power of the IBMC can no longer be controlled with the output voltage control alone.

If we consider the swing equation (6), it can be concluded that the inertial response is created by the power exchange between the power of the mechanical rotor (P_{gov}), which is controlled by the governor, and the power injected to the grid (P_{out}), which is influenced by the output network variables such as frequency and phase angle. Hence, in order to create a proper inertial response, the input power command needs to be regulated to mimic how the output power of SGs exchanges power with the electrical grid according to the power angle. Contrarily, if the powers command of VSR is delivered by methods such as average dc-link voltage control, P_{out} will be independent of the change in the frequency of the output network. Thus the power exchange between the mechanical rotor and the electrical grid of SGs will not be recreated. The power command of VSG control can thus be determined with the help of the equation of the active power flow in a two-bus bar system [48] shown in (8).

$$P_{out} = \frac{V_o V_c}{X_o} sin\delta \tag{8}$$

where V_o is the output voltage amplitude, V_C is the output filter's capacitor voltage amplitude, X_o is the output filter reactance, and δ is the phase angle difference between DG and grid. Assuming V_o, V_c and X to be constant and $\sin\delta \approx \delta$ for a small phase angle, P_{out} is equal to $K\delta$ when $K = V_c V_o / X_o$. However, since the value K of the proposed control is not limited by the physical values of the system like real SGs and can be arbitrarily selected to optimize the system performance, P_{out} of the proposed VSG control can be rewritten as.

$$P_{out} = k_\delta \delta \tag{9}$$

where k_δ is the optimized synchronizing constant, and δ can be determined with the following equation (10).

$$\delta = \int (\omega_m - \omega_{PLL})\, dt \tag{10}$$

With (9)–(10), the active power command for VSR is obtained as depicted in Fig. 8. As for the reactive power command of VSR, it is set to zero for unity power factor operation.

2) THE GENERATION OF THE CURRENT COMMAND FOR FCS-MPC

In the CSI side, the voltage command for the FCS-MPC is obtained with the VSG control scheme in Fig. 8. However, to achieve resonance damping, both voltage and current control must be embedded into a single loop control, as depicted in Fig. 8. Therefore, the current command must be provided for the FCS-MPC. The current command can be determined by considering the relationship between the inverter output voltage, the output current, and the capacitor phase voltage shown in Fig. 1. It can be described in a stationary ($\alpha\beta$) frame with Eq. (11).

$$\boldsymbol{v}_{c,\alpha\beta} = \boldsymbol{v}_{o,\alpha\beta} + \boldsymbol{i}_{o,\alpha\beta}(R_o + j(X_o)) \tag{11}$$

where $\boldsymbol{v}_{c,\alpha\beta}$ is the capacitor voltages, $\boldsymbol{i}_{o,\alpha\beta}$ the output current and $\boldsymbol{v}_{o,\alpha\beta}$ is the output voltages. X_o denotes the filter reactance and R_o denotes filter resistance. If we consider that the $\boldsymbol{v}_{c,\alpha\beta}$ in (11) equals to the voltage command described by E^* and θ^* from the VSG control, the currents references i^*_α and i^*_β can be expressed as illustrated in (12), and they will be used as the current command for the CSI side of the FCS-MPC.

$$\begin{bmatrix} i^*_\alpha \\ i^*_\beta \end{bmatrix} = \boldsymbol{Y} \left\{ \begin{bmatrix} E^* cos\theta^* \\ E^* sin\theta^* \end{bmatrix} - \begin{bmatrix} v_{o,\alpha} \\ v_{o,\beta} \end{bmatrix} \right\} \tag{12}$$

where $\boldsymbol{Y} = \frac{1}{R_o^2 + X_o^2} \begin{bmatrix} R_o & X_o \\ -X_o & R_o \end{bmatrix}$.

3) STABILITY AND TRANSIENT PERFORMANCE ANALYSES

The modification of the VSG control explained in section III-A.1, suggests the use of ω_{PLL} to determine the output power command. However, the dynamic response of the phase-locked loop (PLL), which is given by (13), is lower than the real ω_g and this might affect the performance of the modified VSG control. In order to study the influence of the PLL toward the stability and transient performance of the VSG control, a state-space model for the proposed VSG control (with PLL) is obtained as given in (14)–(20). The model and the transient response of the PLL is well discussed in [49]. The transient response can be described with the following expression.

$$G_{pll}(s) = \frac{\omega_{PLL}(s)}{\omega_g(s)} = \frac{k_{p,pll} s + k_{i,pll}}{s^2 + k_{p,pll} s + k_{i,pll}} \tag{13}$$

Since the dynamic response of the FCS-MPC is fast, the output power is assumed to be equal to the power command. Then the state-space model can be expressed as follows.

$$\begin{cases} \dot{\boldsymbol{x}} = \boldsymbol{A}\boldsymbol{x} + \boldsymbol{B}u + \boldsymbol{E}w \\ \boldsymbol{y} = C\boldsymbol{x} \end{cases} \tag{14}$$

where $\boldsymbol{x}$, u, w and $\boldsymbol{y}$ are states, input, disturbance and outputs vectors, respectively, and

$$\boldsymbol{y} = \begin{bmatrix} \Delta\omega_m & \Delta P_{out} & \Delta\omega_{PLL} \end{bmatrix}^T \tag{15}$$

$$\boldsymbol{x} = \begin{bmatrix} \Delta\omega_m & \Delta P_{out} & \int \Delta\delta_{err,pll} & \Delta\delta_{err,pll} \end{bmatrix}^T$$

$$u = \Delta P_0$$

$$w = \Delta\omega_g \tag{16}$$

$$\boldsymbol{A} = \begin{bmatrix} \frac{-(k_p+D)}{J\omega_o} & \frac{-1}{J\omega_o} & \frac{Dk_{i,pll}}{J\omega_o} & \frac{Dk_{p,pll}}{J\omega_o} \\ k_\delta & 0 & -k_\delta k_{i,pll} & -k_\delta k_{p,pll} \\ 0 & 0 & 0 & 1 \\ 0 & 0 & -k_{i,pll} & -k_{p,pll} \end{bmatrix} \quad (17)$$

$$\boldsymbol{B} = \begin{bmatrix} \frac{1}{J\omega_o} & 0 & 0 & 0 \end{bmatrix}^T \quad (18)$$

$$\boldsymbol{E} = \begin{bmatrix} 0 & 0 & 0 & 1 \end{bmatrix}^T \quad (19)$$

$$\boldsymbol{C} = \begin{bmatrix} 1 & 0 & 0 & 0 \\ 0 & 1 & 0 & 0 \\ 0 & 0 & k_{i,pll} & k_{p,pll} \end{bmatrix} \quad (20)$$

where $\delta_{err,pll} = \int (\omega_g - \omega_{PLL})dt$.

It is clear that the poles of $Y(s)/W(s)$ transfer function are available in the eigenvalues of $\boldsymbol{A}$. The loci of eigenvalues of $\boldsymbol{A}$ with a variation of $k_{i,pll}$ is shown in Fig. 10 when $k_{p,pll}$ is selected according to [49]. First, it can be seen in Fig. 10 that all the poles of the system located on the left half of the s-plane, which implies that the system is stable. It is also shown in Fig. 10 that if the PLL has a rather quick dynamic response (if $k_{i,pll}$ is large enough), the effect of the third pole that locates near the dominant poles will be lessened as it is located farther to the left of the two dominant poles. In this case, the response of the system will be mostly defined by the two dominant poles, as can be described with the following expressions [50]:

$$\omega_n = \sqrt{\frac{k_\delta}{J\omega_0}} \quad (21)$$

$$\zeta = \frac{k_p + D}{2\sqrt{k_\delta J\omega_0}} \quad (22)$$

where ω_n is the undamped natural frequency, and ζ is the damping ratio. However, as shown in Fig. 10, even with a properly designed PLL with a fast dynamic response, the locations of the two additional poles are not far enough to the left of dominant poles, their effect cannot be totally neglected. Hence, the response of P_{out} will be slower than the previous VSG controls, thus finally results in a less inertial response. This can be interpreted as a delay effect of the PLL, because unlike the VSG system with an energy storage element, P_{out} of the proposed control is not dispatched directly from the energy storage element. It is instead regulated by the power command, which depends on the ω_{PLL}. This is crucial for VSG control, as P_{out} needs to react quickly to the power imbalance in order to create a proper inertial response. Since k_δ of the proposed VSG control is not limited by the physical values of the system and can be arbitrarily selected, we can find an optimal value of k_δ by studying the effect of adjusting k_δ with the loci of eigenvalues of $\boldsymbol{A}$, as shown in Fig. 11. It indicates that increasing k_δ leads to an increase in ω_n. This can compensate for the delay effect of the PLL. Hence, $k_\delta = 2.5^* V_c V_o / X_o$ is chosen for the proposed control.

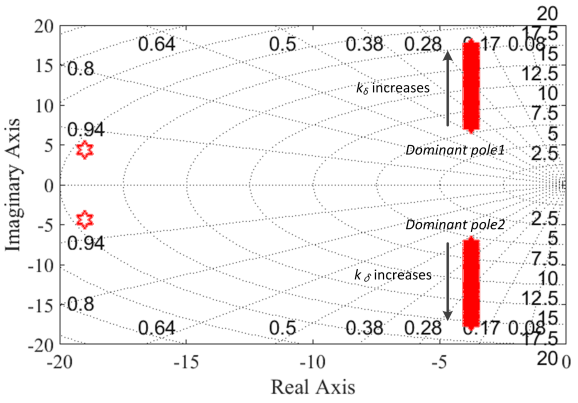

FIGURE 11. Eigenvalue loci with changing of k_δ.

B. FCS-MPC DESIGN

In this work, the FCS-MPC is chosen for the implementation of VSG control instead of PWM-methods based on two main reasons. First, the modulation index of CSI PWM is not adjustable because the zero current vectors cannot be used in IBMC topology, as discussed in subsection II-B. Without zero current vectors, the PWM cannot control the amplitude of the output voltage according to the voltage command of VSG control. This implies that, with the PWM-based method, the ability of VSG control to regulate reactive power according to the Q-V droop cannot be recreated, and the amplitude of the output voltage cannot be maintained during islanded mode as discussed in Section II-C. Second, although the output amplitude of CSI can be indirectly controlled through the modulation of VSR PWM, proper tracking of voltage command cannot be ensured due to the complex coupling between the rectifier and the inverter controls, as discussed in section II. The FCS-MPC, on the other hand, utilizes the system model and the real-time values of the system to determine the optimized converter's physical switching states directly. Thus it enables proper tracking of voltage and current commands even without the use of zero current vectors of CSI.

The FCS-MPC is also applied in the VSR side of the IBMC because of the faster dynamic response of the FCS-MPC compared to the PWM-based methods. This is crucial for the proposed VSG control, as the inertial power is provided from the power control of the VSR side.

1) IBMC SYSTEM MODEL

In order to use MPC to forecast the future values of the system variables, first, the mathematical model of the system is required. Therefore, the adopted models for both CSI and VSR sides will be explained in this section.

To realize a DG that can operate in both grid-connected and islanded modes, the inverter output voltage and inverter current controls should be the objectives of MPC for the CSI side. Thus, the model of a three-phase CSI with output CL-filter,

as depicted in Fig. 1 is utilized to forecast the voltage and current outputs of the system. This model can be described in $\alpha\beta$-frame using capacitor dynamics equation (23) and inductance dynamics equation (24).

$$C\frac{d\boldsymbol{v_c}}{dt} = \boldsymbol{i}_{inv} - \boldsymbol{i}_o \tag{23}$$

$$L_o\frac{d\boldsymbol{i_o}}{dt} = \boldsymbol{v}_c - \boldsymbol{v}_o \tag{24}$$

where $\boldsymbol{v_c} = \left[v_{c,\alpha} v_{c,\beta}\right]^T$, $\boldsymbol{v}_o = \left[v_{o,\alpha} v_{o,\beta}\right]^T$, $\boldsymbol{i}_{inv} = \left[i_{inv,\alpha} i_{inv,\beta}\right]^T$ and $\boldsymbol{i}_o = \left[i_{o,\alpha} i_{o,\beta}\right]^T$ are capacitor voltage, output voltage, inverter current, and the output current, respectively. These equations can be rewritten as follows (25):

$$\dot{\boldsymbol{x}} = \boldsymbol{A}\boldsymbol{x} + \boldsymbol{B}\boldsymbol{v}_o + \boldsymbol{B}_d\boldsymbol{i}_o \tag{25}$$

where $\boldsymbol{x} = \begin{bmatrix} i_{o,\alpha} \\ i_{o,\beta} \\ v_{c,\alpha} \\ v_{c,\beta} \end{bmatrix}$, $\boldsymbol{A} = \begin{bmatrix} 0 & 0 & \frac{1}{L_o} & 0 \\ 0 & 0 & 0 & \frac{1}{L_o} \\ \frac{1}{C} & 0 & 0 & 0 \\ 0 & \frac{1}{C} & 0 & 0 \end{bmatrix}$, $\boldsymbol{B} = \begin{bmatrix} -\frac{1}{L_o} & 0 \\ 0 & -\frac{1}{L_o} \\ 0 & 0 \\ 0 & 0 \end{bmatrix}$. and. $\boldsymbol{B_d} = \begin{bmatrix} 0 & 0 \\ 0 & 0 \\ -\frac{1}{C} & 0 \\ 0 & -\frac{1}{C} \end{bmatrix}$.

A discrete-time model of the system derived from (25), using the general forward-difference Euler formula, for a sampling time T_s can be expressed in (26).

$$\boldsymbol{x}\,(k+1) = \boldsymbol{A}_q\boldsymbol{x}\,(k) + \boldsymbol{B}_q\boldsymbol{v}_o\,(k) + \boldsymbol{B}_{dq}\boldsymbol{i}_o\,(k) \tag{26}$$

where $\boldsymbol{A}_q = e^{\boldsymbol{A}T_s}$, $\boldsymbol{B_q} = \int_0^{T_s} e^{\boldsymbol{A}\tau}\boldsymbol{B}d\tau$ and $\boldsymbol{B}_{dq} = \int_0^{T_s} e^{\boldsymbol{A}\tau}\boldsymbol{B}_d d\tau$. From (25)–(26), it can be seen that the future values $\boldsymbol{v}_c(k+1)$ and $\boldsymbol{i}_o\,(k+1)$ can be determined according to inverter stage current $\boldsymbol{i}_{inv}\,(k)$. For each active current vectors (SC1-SC6) of CSI, the inverter stage current $\boldsymbol{i}_{inv}\,(k)$ is defined as follows:

$$\boldsymbol{i}_{inv}\,(k) = [\,S_{ap} - S_{an} \quad S_{bp} - S_{bn} \quad S_{cp} - S_{cn}\,]^T i_{DC} \tag{27}$$

where S_{ap}, S_{bp}, S_{cp}, S_{an}, S_{bn}, S_{cn} represent the switching states of the six switches in the inverter stage, as depicted in Fig. 1. The value of the switching state consists of 1 and 0, for which it represents the closed and open states, respectively. As shown in (27), although only active current vectors (SC1-SC6) can be used in the CSI of IMBC, by predicting the inverter output variables corresponding to all possible current vectors, the switching state that produces the desired amplitude and phase of the inverter output variables can be found. In contrast to the modulation method of the PWM-based control, which only follows the phase angle reference and only utilizes two nearest space vectors to the reference phasor to generate output current, the FCS-MPC certainly has more freedom to select an optimal switching state to fulfill the inverter control goal.

To accomplish the grid frequency supporting feature of VSG, the input active power must be controllable, as active power and grid frequency have a direct relationship. Additionally, the reactive power should be kept at zero to achieve unity power factor. Therefore, the control objectives of MPC for the VSR side are active and reactive power controls. The model of a three-phase voltage source rectifier with input L-filter depicted in the VSR side of IBMC in Fig. 1 is utilized for input active and reactive powers predictions. This model can be derived in $\alpha\beta$-frame with inductance dynamics equation (28).

$$\boldsymbol{v}_s = \boldsymbol{v}_r + \boldsymbol{i}_s R_i + L_i\frac{\mathrm{d}\boldsymbol{i}_s}{\mathrm{d}t} \tag{28}$$

where $\boldsymbol{v}_s$ is the source voltage, $\boldsymbol{v}_r$ is the rectifier voltage, $\boldsymbol{i}_s$ is the source input current and R_i is the input filter resistor. Derived from (28), the rectifier instantaneous input active and reactive powers from the source can be described with the following equations.

$$P_{in} = \frac{3}{2}Re\left\{\boldsymbol{v}_s\bar{\boldsymbol{i}_s}\right\} = \frac{3}{2}\left(v_{s\alpha}i_{s\alpha} + v_{s\beta}i_{s\beta}\right) \tag{29}$$

$$Q_{in} = \frac{3}{2}Im\left\{\boldsymbol{v}_s\bar{\boldsymbol{i}_s}\right\} = \frac{3}{2}\left(v_{s\alpha}i_{s\beta} - v_{s\beta}i_{s\alpha}\right) \tag{30}$$

where $\bar{(\cdot)}$ indicates the complex conjugate operation. The equations (29)-(30) can be rewritten in discretized forms as follows [43].

$$P_{in}(k+1) = T_s\left[-\frac{R_i}{L_i}P_{in}(k) - \omega_{in}Q_{in}(k) + \frac{3}{2L}\left(\left|\boldsymbol{v}_s^2\right| - Re\left\{\boldsymbol{v}_s\overline{\boldsymbol{v}_r}\right\}\right)\right] + P_{in}(k) \tag{31}$$

$$Q_{in}(k+1) = T_s\left[\omega_{in}P_{in}(k) - \frac{R_i}{L_i}Q_{in}(k) - \frac{3}{2L}Im\left\{\boldsymbol{v}_s\overline{\boldsymbol{v}_r}\right\}\right] + Q_{in}(k) \tag{32}$$

where $P_{in}(k+1)$ and $Q_{in}(k+1)$ are the forecasted active and reactive powers, respectively and ω_{in} is the input source voltage frequency. Thus, the future value of input active and reactive powers of the DG for all voltage vectors can be predicted using the measured values of source voltage, source current and system parameters such as R_i L_a and ω_{in}, and a set of possible rectifier voltages. The rectifier voltage for each voltage vectors (SV0-SV7) is defined according to the following expression:

$$\boldsymbol{v}_r\,(k) = [\,S_{Ap} - S_{An}\;S_{Bp} - S_{Bn}\;S_{Cp} - S_{Cn}\,]^T u_{DC} \tag{33}$$

where S_{Ap}, S_{Bp}, S_{Cp}, S_{An}, S_{Bn}, S_{Cn} represent the switching states of the six switches in the rectifier stage, whose value is 1 or 0 for the closed state and open state, respectively.

To prevent a short circuit in the antiparallel diodes of VSR, the dc-link voltage must always be positive. To ensure this, we must predict the value of dc-link voltage for each switching state using the capacitor voltages $\boldsymbol{v_c}$, which can be done according to the following equations.

$$u_{DC} = [\,S_{ap} - S_{an} \quad S_{bp} - S_{bn} \quad S_{cp} - S_{cn}\,] * \boldsymbol{v}_c \tag{34}$$

2) COST FUNCTION DEFINITION

Contrarily to classical control schemes, the presence of the cost function allows the FCS-MPC to take into account a number of control goals, and to control different state variables simultaneously. Therefore, it is highly relevant to define the cost function properly. For the control of IBMC, variable quantities of both sides of the converter must be considered to make the whole system operate correctly.

In the CSI side, the control system is set to track the voltage and current references, simultaneously. This can be achieved by defining a cost function as follows.

$$g_{CSI} = k_v(\boldsymbol{v}_{c,\alpha\beta,pu}\,(\mathrm{k}+1) - \boldsymbol{v}^*_{\alpha\beta,pu})^2 + k_i(\boldsymbol{i}_{f,\alpha\beta,pu}\,(\mathrm{k}+1) - \boldsymbol{i}^*_{\alpha\beta,pu})^2 + g_m \quad (35)$$

where, $\boldsymbol{v}^*_{\alpha\beta} = \begin{bmatrix} v^*_\alpha & v^*_\beta \end{bmatrix}^T$ is the reference vector of the capacitor voltage, $\boldsymbol{i}^*_{\alpha\beta} = \begin{bmatrix} i^*_\alpha & i^*_\beta \end{bmatrix}^T$ is the reference vector of the inductor current, $\boldsymbol{v}_{c,\alpha\beta}(k+1) = \begin{bmatrix} v_{c,\alpha} & v_{c,\beta} \end{bmatrix}^T$ is the predicted capacitor voltage and $\boldsymbol{i}_{f,\alpha\beta}(k+1) = \begin{bmatrix} i_{f,\alpha} & i_{f,\beta} \end{bmatrix}^T$ is the predicted inductance current, and the subscript *pu* indicates the per-unit value. g_m is a constraint, which is included in the cost function to ensure that dc-link voltage never becomes negative. It can be defined with the equation (36).

$$g_m = \begin{cases} 10^8, & u_{DC}(k+1) < 0 \\ 0, & u_{DC}(k+1) \geq 0 \end{cases} \quad (36)$$

In the VSR side, the control objectives are to control input active and reactive power according to the input commands. This can be achieved by defining the cost function as follows

$$g_{VSR} = (P_{in}(k+1) - P^*_{in})^2 + (Q_{in}(k+1) - Q^*_{in})^2 \quad (37)$$

where, P^*_{in} and Q^*_{in} are the input active and reactive power commands, respectively.

Although the FCS-MPC is capable of controlling different variables at the same time through the modification of the cost function, the tuning of the weighting parameters is a highly complex task when a number of terms exist in the cost function. This issue is considered as one of the most critical open topics for the FCS-MPC. In the literature, different approaches have been thoroughly analyzed, and several solutions have been proposed [44]–[47].

In this paper, the weighting parameters exist in cost functions (35) and (37). However, the controls of active and reactive powers in (37) are equally important, and the weighting parameters can be omitted from the cost function. In the case of CSI, to properly tune the weights in (35), the system has been initially simulated in a steady-state condition ($P^*_{in} = 5\,kW, Q^*_{in} = 0\,var$) using the PSCAD/EMTDC software. The ratio between the weighting parameters k_v and k_i has been arbitrarily set equal to 1:1. Subsequently, the THD of the output currents during steady-state in the grid-connected operation and the ability of the controller to synchronize with the grid have been analyzed for different weighting parameter ratios, as concluded in Table 2. Conclusively, a higher ratio of k_i compared to k_v helps to reduce the current THD. However, as k_i keeps increasing, the controller's ability to track voltage command worsens, which leads to a failure in grid synchronization. Hence $k_v : k_i$ equal to 1:3 has been selected for the proposed controller.

TABLE 2. FCS-MPC weight parameter tuning.

k_v: k_i ratio	Current *THD*	Synchronization
1:1	10 %	OK
1:2	5 %	OK
1:3	2.5 %	OK
1:4	-	Failed

3) FILTER RESONANCE DAMPING

To ensure proper operations, the IBMC requires an inductive input filter on the VSR and a capacitive output filter on the CSI. However, in order to improve the quality of the waveforms, *CL*-filter is usually preferred. Nevertheless, the presence of resonance frequency has to be taken into account since the FCS-MPC possesses a variable switching frequency. It might generate harmonics components at the resonant frequency of *CL*-filter at a certain operating point. However, this will result in resonance, if only the output inverter current $\boldsymbol{i}_o\,(s)$ is directly controlled, whereas the capacitor voltage $\boldsymbol{v}_c(s)$, is indirectly controlled by the current and thus highly dependent on filter impedances.

The proposed FCS-MPC utilizes a multivariable system to control both $\boldsymbol{v}_c(s)$ and $\boldsymbol{i}_o\,(s)$ simultaneously. This is different from conventional cascade control of voltage and current, where settling time of the inner loop must be significantly faster than the settling time of the outer loop. Therefore, at the resonant frequency where $\boldsymbol{v}_c(s)$ and $\boldsymbol{i}_o\,(s)$ are oscillating with the same dynamics; the control of the outer loop is not fast enough to provide a damping effect. Contrarily, the multivariable control of the FCS-MPC is conducted at the same bandwidth. This ensures that the regulation of $\boldsymbol{v}_c(s)$ can damp the distortion caused by the harmonics of $\boldsymbol{i}_o\,(s)$ and the control of $\boldsymbol{i}_o\,(s)$ is able to reduce the disturbance caused by the harmonics of $\boldsymbol{v}_c(s)$. Hence, by controlling both *CL*-filter voltage and current at the same instances, the frequency response of the filter is no longer influenced by its impedance alone. Thus the uncontrolled resonant energy oscillation between the inductances and the capacitance is effectively avoided. This concept has been successfully applied in the FCS-MPC-based grid-connected VSI in [36], whereas similar concepts were also proposed in [37]–[39] for the grid-connected FCS-MPC-based AC/DC converter.

IV. SIMULATION AND DISCUSSION

In order to evaluate the performance of the proposed control scheme, simulation-based comparative studies between the proposed scheme and the investigated existing method are performed in the PSCAD/EMTDC environment. The simulation parameters are given in Table 3, In order to

TABLE 3. Simulation parameters.

Parameter	Value	Parameter	Value
S_{base}	5 kVA	J	$0.28\ kg \cdot m^2$
k_p	40 pu	D	200 pu
V_{based}	200 V	k_δ	70000
$T_{i,pll}$	0.5 s	$k_{p,pll}$	0.1
$\omega_{base} = \omega_{grid}$	376.99 rad/s		

generate a comparable average switching frequency with the PWM-based method, the sampling frequency for the VSR ($f_{s,vsr,mpc}$) is selected at 40 kHz and the sampling frequency for the CSI $f_{s,csi,mpc}$ of the FCS-MPC-based control is selected at 20 kHz, respectively. This brings about the measured average switching frequency around 19 kHz for VSR and 7 kHz for CSI of the FCS-MPC-based control, respectively.

A. NORMAL OPERATION

The performance of the proposed VSG control for the IBMC is verified with simulations of the test circuit displayed in Fig. 8. Initially, the DG system is connected to the grid with the reference active power of DG (P_0) equals 4 kW and reference reactive power of DG (Q_0) equals 1 kvar. The power commands are changed to 5 kW and 0 kvar at $T = 3$ s. The DG system is then set to operate in islanded mode at $T = 5$ s. The load initially connected to the system is 3 kW + 1 kvar, and it is increased to 5.5 kW + 0.05 kvar at $T = 7$ s. The phase-A input current and the phase-a output current during the grid-connected operation of the proposed method in the event of power command changing at $T = 3$ s is illustrated in Fig. 12. The figure shows that the input and output current waveforms are smoothly changed when the power command is changed. The zoom-ups of the dc-link voltage, the input current, the dc-link current, and the output current for the grid-connected operation are depicted in Fig. 13. This figure shows that both input and output current waveforms are sinusoidal, and neither voltage nor current spikes are observed on the dc capacitor. Therefore the converter is operating properly.

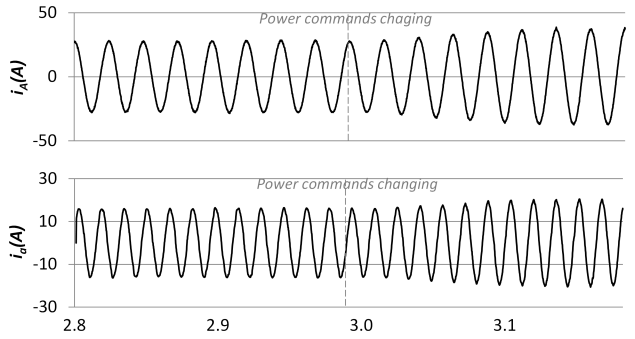

FIGURE 12. Simulation results of transient waveforms of the phase-A input current, and the phase-a output current of the proposed method during power command changing in the grid-connected mode.

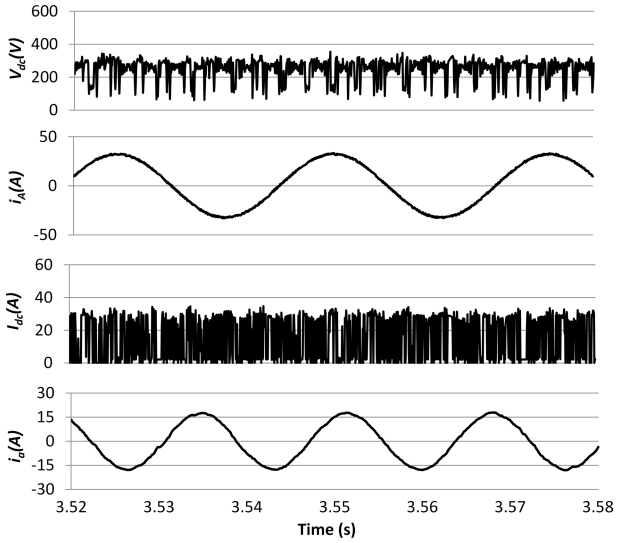

FIGURE 13. Simulation results of steady-state waveforms of the the dc-link voltage, the phase-A input current, the dc-link current, and the phase-a output current of the proposed method during the grid-connected mode, from top to bottom, respectively.

The proposed VSG-based control is inherently capable of islanded operation like a traditional SG. To illustrate this feature, the phase-A input current, the phase-a output voltage, and the phase-a output current are displayed in Fig. 14. This figure clearly shows that the controller is capable of riding through the grid islanding while producing sinusoidal waveforms of voltage and current in both modes of operation. The output active and reactive powers, the output frequency, and the output voltage amplitude for the whole simulation are illustrated in Fig. 15. It can be seen that the system quickly and seamlessly commutates from the grid-connected mode into the islanded mode, supplying the required 3 kW + 1 kvar of power to the local load. The system is also able to react

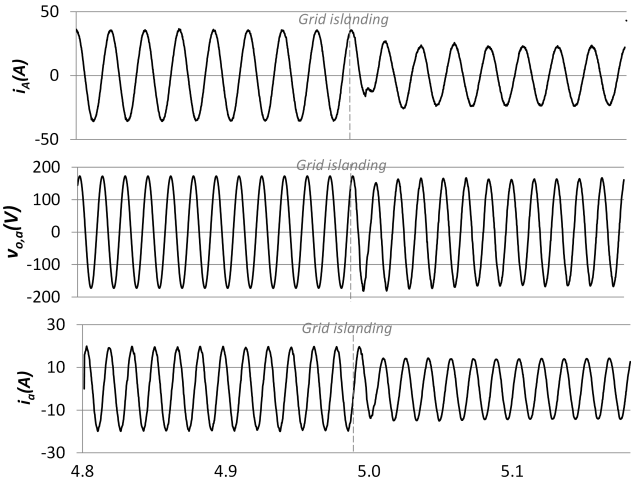

FIGURE 14. Simultion results of transient waveforms of the phase-A input current, the phase-a output voltage, and the phase-a output current of the proposed method during grid islanding.

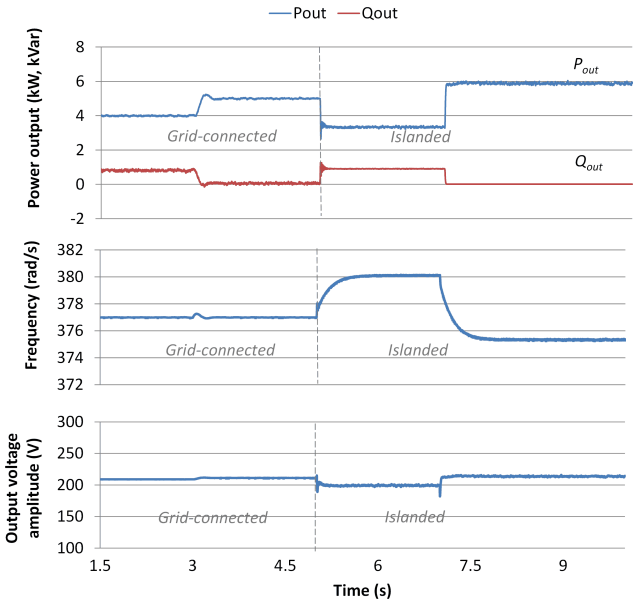

FIGURE 15. Simulation results of the output active and reactive power, the output frequency, and the output voltage amplitude of the proposed control scheme, from top to bottom, respectively.

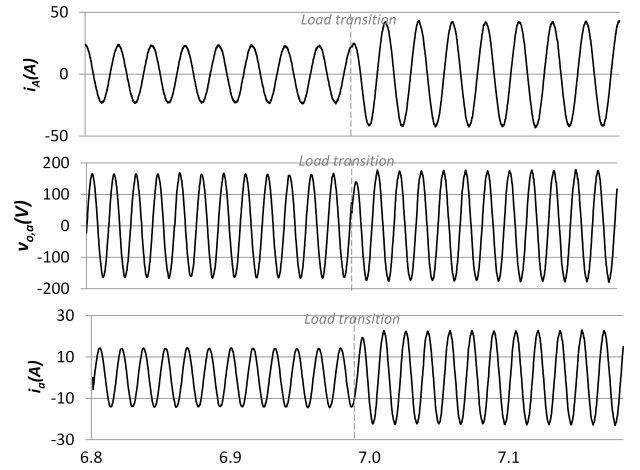

FIGURE 16. Simulation results of transient waveforms of the phase-A input current, the phase-a output voltage, and the phase-a output current of the proposed method during load transition in the islanded.

to change in load during islanded operation, as evidenced in Figs. 15 and 16, where waveforms of the phase-A input current, the phase-a output voltage, and the phase-a output current are depicted. The output frequency and the output active power of the control system in Fig. 15, are illustrating how the system is settling to operate at a different frequency according to the droop characteristic, whereas the output voltage amplitude of the system is maintained around the nominal value (V_{based}) throughout the operation. Furthermore, the change in output frequency during the load transition in islanded mode demonstrates the inertial response of the controller, as the output frequency slowly decreases from around 378.5 rad/s to around 376 rad/s. The reduction of frequency occurs for around 1 s until the new frequency set point is reached. This is a typical VSGs performance, as analyzed in [26], [27]. The zoom-ups of the dc-link voltage, the input current, the dc-link current, the phase-a output voltage, and the output current for islanded operation illustrated in Fig. 17, indicates that current and voltage are almost sinusoidal even without a passive damping resistor.

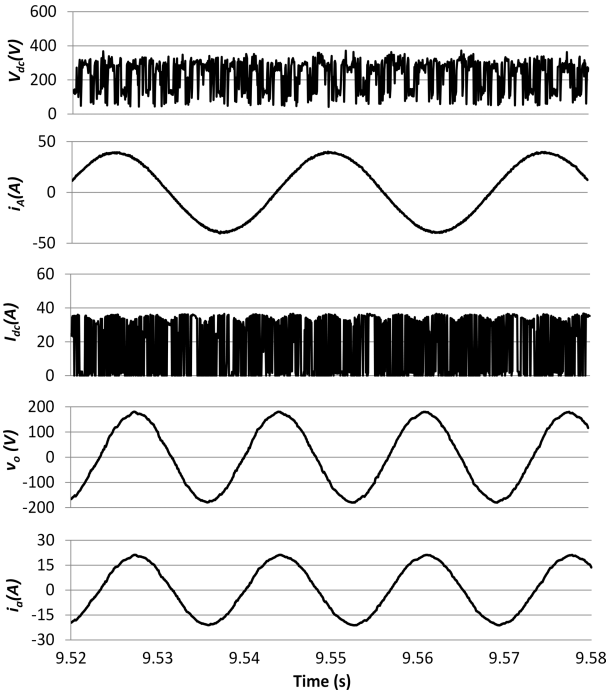

FIGURE 17. Simulation results of steady-state waveforms of the dc-link voltage, the phase-A input current, the dc-link current, the phase-a output voltage, and the phase-a output current of the proposed method during the islanded mode, from top to bottom, respectively.

Lastly, the THD of input and output currents of the proposed control during steady-state are concluded in Table 4. Compared to Table 1, it is clearly shown that the proposed control can achieve comparable and even superior resonance damping ability compared to the exiting method with a damping resistor.

TABLE 4. Current THDs for the proposed scheme.

Condition	Output current *THD*	Input current *THD*
The proposed method during grid-connected mode	≈3 %	≈1.5 %
The proposed method during islanded mode	≈2 %	≈1 %

B. OPERATION IN THE PRESENCE OF MODEL UNCERTAINTY

In practice, the real values of the inductance and capacitance could deviate from the supposed ones, especially on the grid side due to the presence of the line impedance. Here, to explore the robustness of the proposed control, the performance of the proposed control scheme is examined when the

model used for prediction is not accurate. The simulations of the test circuit shown in Fig. 8 are conducted again with mismatches between the parameters used for prediction and real system parameters. In the first case, the values of output filter inductance and capacitance are changed from 3 mH and 30 μF to 2.5 mH and 25 μF, respectively. Then in the second case, the inductance and capacitance are changed to 5 mH and 40 μF, respectively. The parameters used for prediction and other parameters are the same as the previous case. The output active and reactive powers, the output frequency, and the output voltage amplitude of Case 1 and Case 2 are illustrated in Fig. 18. and 19, respectively. For both cases, the predictive controller is able to achieve proper control similar to the case when the model of the system is accurate. Hence, we can conclude that the proposed FCS-MPC is not sensitive to uncertainty in prediction parameters.

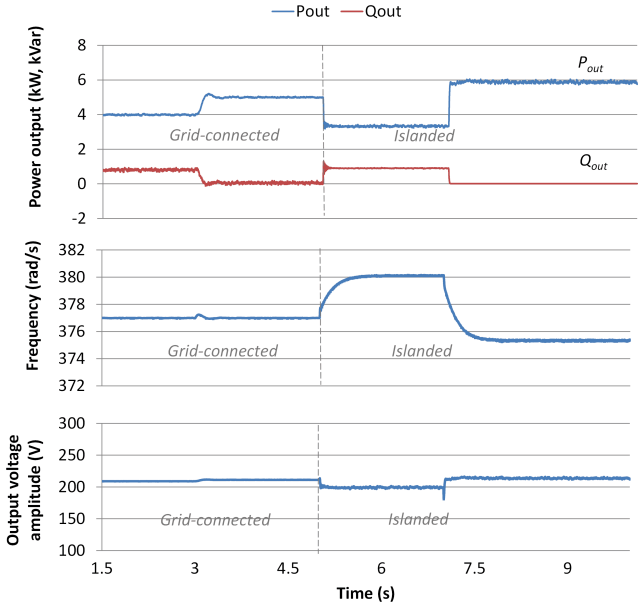

FIGURE 18. Simulation results of the output active and reactive power, the output frequency, and the output voltage amplitude of the proposed control scheme with uncertainty in the prediction model (case1).

C. INERTIAL RESPONSE

To demonstrate the inertial response of the VSG when the load is increased from 3 kW + 1 kvar to 5.5 kW + 0.05 kvar during the islanded operation, the simulations of the test circuit displayed in Fig. 8 are conducted again with the same simulation parameters. However, different values of parameter J are simulated in order to study the responses of the output active power and the converter frequency, as shown in Fig. 20. From this figure, it can be seen how the frequency of the VSG with larger inertia constant is more reluctant to change, and an increase in the inertia constant leads to an increase in settling-time of the output frequency. However, it is indicated in the same figure that larger inertia constants result in larger ripples of the active power in steady-state. Nevertheless, from these results, we can clearly conclude that the proposed VSG control is capable of providing an inertial

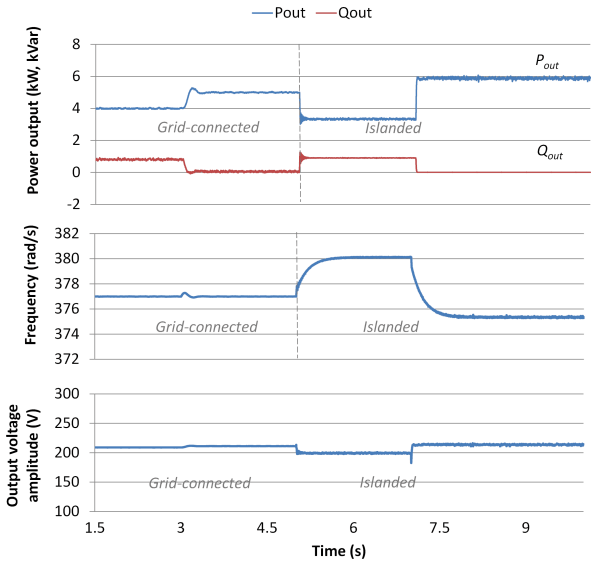

FIGURE 19. Simulation results of the output active and reactive power, the output frequency, and the output voltage amplitude of the proposed control scheme with uncertainty in the prediction model (case2).

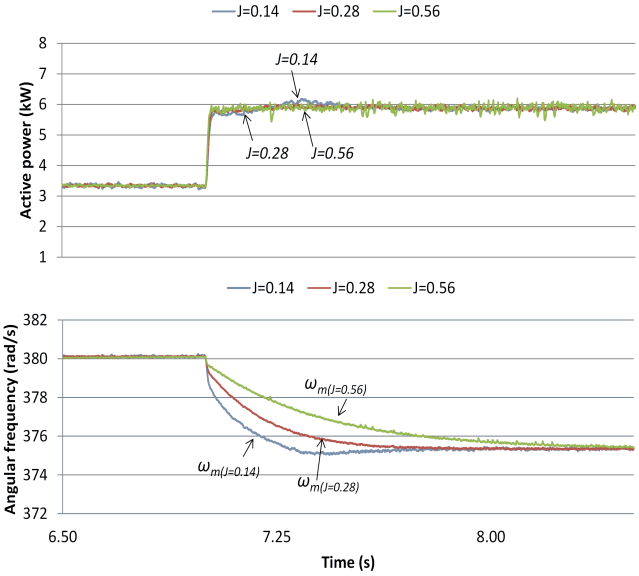

FIGURE 20. Simulation results of tThe measured output frequency and output active power of the proposed method when the output load is changed from 3 kW + 1 kvar to 5.5 kW + 0.05 kvar during islanded operation mode.

response even without the presence of an energy storage element. It is also noticeable that the transient response of P_{out} is slightly lower than the typical VSGs performance analyzed in [26], [27] due to the delay effect of the PLL. This effect can be lessened with an increased k_δ, as discussed in the stability analysis of section III-B.

V. EXPERIMENTAL VERIFICATION

To verify the simulation results, a scaled-down version of the simulation circuit depicted in Fig. 8 is conducted with the testbed illustrated in Fig. 21. Three-phase 30 Hz / 40 V

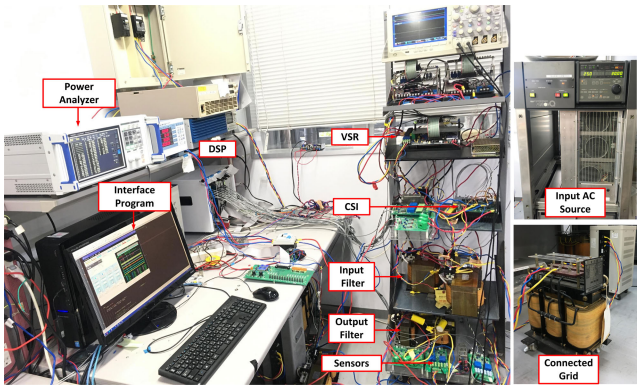

FIGURE 21. Testbed for experimental verification.

(line-to-line RMS) input ac-source and 60 Hz / 60 V (line-to-line RMS) stepped-down grid voltage are considered for the experiment. The parameters indicated in Fig. 1 were respectively realized as follows, $L_i = 7$ mH, $R_i = 0.1\ \Omega$, $L_o = 4$ mH, $R_o = 0.1\ \Omega$, $C = 30\ \mu$F and 2 μF for fictitious dc-link capacitor. These values are chosen from those available in the laboratory. S_{base} and V_{base} are changed to 150 W and 60 V, respectively. k_δ is set to $2.5{*}V_{base}^2/X_o$, whereas other control parameters are adopted from the simulation study, as concluded in Table 3. The experiment scenarios are adopted from the simulations. First, the IBMC is set to operate in grid-connected mode, and then it is islanded from the grid and operates independently to supply local load. This is done to verify the grid-forming ability of the proposed control. Then the load changing is performed in the islanded operation to demonstrate the inertial behavior of the controller. Both the CSI and the VSR are controlled by a digital control unit Myway PE-Expert IV, and the presented data are internal variables of the control unit, which are recorded using the embedded function of PE-View X, the software interface of Myway PE-Expert IV, which can illustrate 100k data per second with 14-bit resolution for 16 channels. It is notable that the oscilloscope presented in Fig. 21 is only used for monitoring the synchronization process of the proposed control system based AC-source with the grid during the experiment. Additionally, HIOKI PW6001 Power analyzer was used to measure the THDs. To imply the FCS-MPC-based control, the sampling frequency for the VSR ($f_{s,vsr,mpc}$) is selected at 35 kHz for the CSI $f_{s,csi,mpc}$ at 20 kHz, respectively, which results in variable switching frequency with average values around 15 kHz for VSR and 10 kHz for CSI in the steady state condition.

By comparing the experimental results displayed in Figs. 22 and 23 to the simulation results displayed in Figs. 13 and 17, it can be concluded that all comments on simulation results still stand for the experimental results. The dc-link voltage, the phase-A input current, the dc-link current, and the phase-a output current for the grid-connected operation are depicted in Fig. 22. This figure shows that both input and output current waveforms are sinusoidal. Additionally, the measured THDs up to the 50th order are also displayed in Fig. 22. It indicates that the THDs of the input

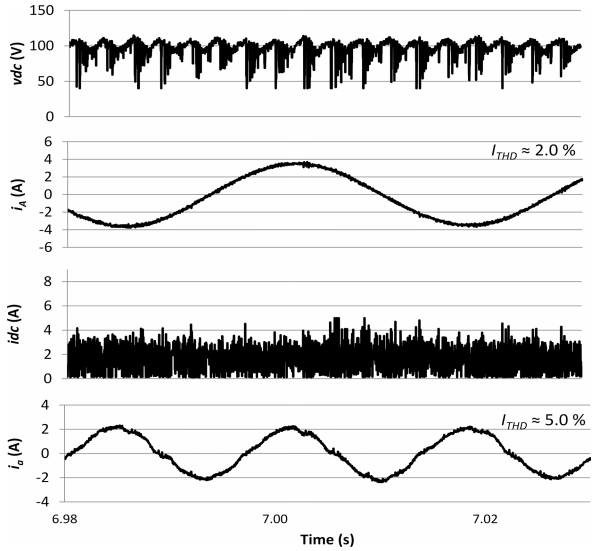

FIGURE 22. Experimental results of steady-state wavwforms of the dc-link voltage, the phase-A input current, the dc-link current, and the phase-a output current of the proposed method during the grid-connected mode, from top to bottom, respectively.

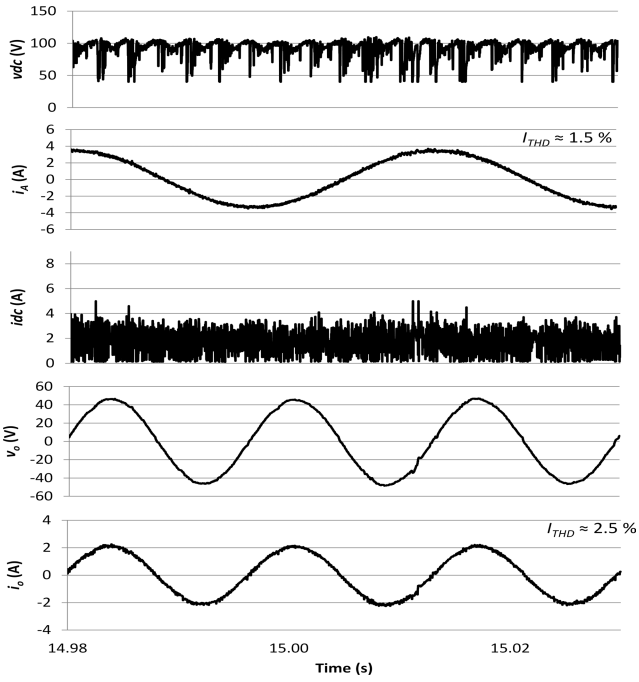

FIGURE 23. Experimental results of steady-state wavwforms of the dc-link voltage, the phase-A input current, the dc-link current, the phase-a output voltage, and the phase-a output current of the proposed method during the islanded mode, from top to bottom, respectively.

and output currents are around 2.0% and 5.0%, respectively. This approves the results of the simulation study that the low order harmonic distortion due to the effect of *CL*-filter resonance can be suppressed by the multivariable control of filter voltage and current. Hence, the THDs of around 5.0% can be achieved even without a passive damping resistor. The dc-link voltage, the phase-A input current, the dc-link current,

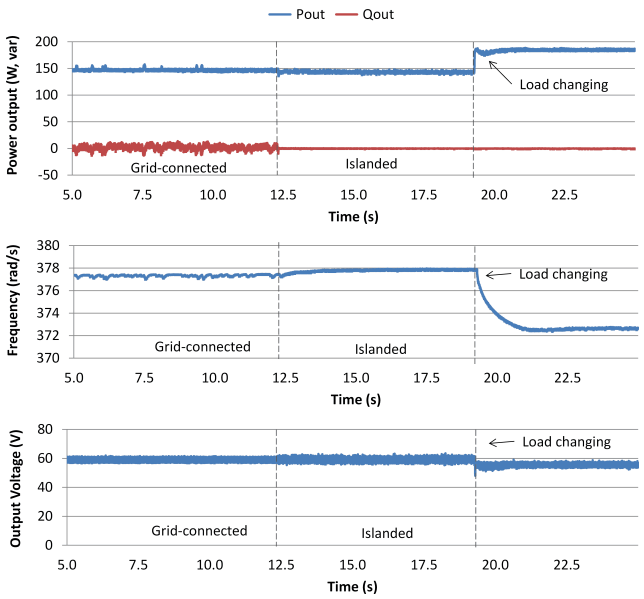

FIGURE 24. Experimental results of the output active and reactive power, the output frequency, and the output voltage amplitude of the proposed method during the grid connected mode, islanded mode and load changing transition in islanded mode from top to bottom, respectively.

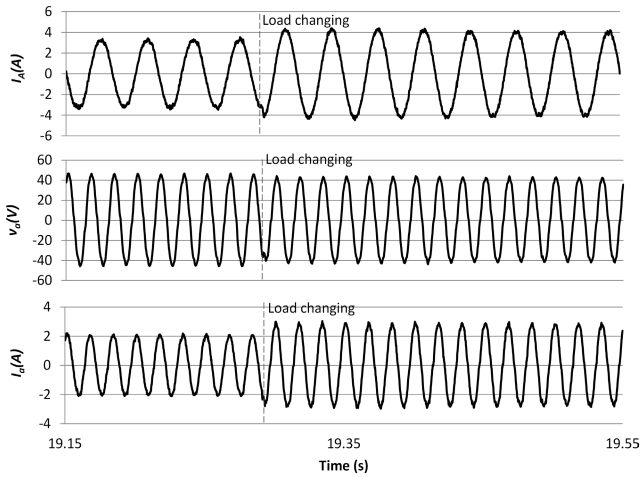

FIGURE 25. Experimental results of transient waveforms of the phase-A input current, the phase-a output voltage, and the phase-a output current of the proposed method during load transition in the islanded.

the phase-a output voltage, and the phase-a output current for the islanded operation illustrated in Fig. 23 indicates that current and voltage are also sinusoidal during islanded operation. The even lower THDs than grid-connected operation are observed for both input and output currents, which amount around 1.5% and 2.5%, respectively.

The output active and reactive powers, the output frequency, and the output voltage amplitude throughout the experiment scenarios are illustrated in Fig. 24. The input active and reactive powers are set to follow the reference values of $P_{in}^{*} = 150\,W$ and $Q_{in}^{*} = 0\,var$. It can be seen that the system quickly and seamlessly transfers from the grid-connected mode into the islanded mode, supplying the power to a 20 Ω local load, whereas the output voltage amplitude of the system is maintained around the nominal value ($60V$) throughout the operation. The system is also able to react to the load changing during islanded operation when another star-connected 50 Ω local load is connected, as shown in Fig. 24 at $T \approx 19$ s and Fig. 25, where waveforms of the phase-A input current, the phase-a output voltage, and the phase-a output current are depicted. The results of the output frequency and the output active power verify the characteristic of VSG control, as discussed in section IV. Hence, the experimental results clearly validate the effectiveness of the proposed control scheme.

VI. CONCLUSIONS

The investigation on the IBMC has shown that the relevant existing control method is not explicitly designed for DG applications, and shortcomings such as the incapability of both grid-connected and islanded operation, the lack of virtual inertia, and the generation of distorted output current, exist in the control system. To solve these problems, a novel control scheme based on multivariable FCS-MPC for the implementation of VSG is proposed in this paper.

Comparative studies between the proposed control schemes and the existing method performed in PSCAD/EMTDC simulation have demonstrated that the proposed grid-forming control scheme offers many advantages over the existing methods, which utilize a grid-following strategy. For instance, thanks to the deployment of the proposed VSG control, the controller can provide the inertia property from the power source to support the grid frequency stability and is also capable of operating independently in islanded operation, maintaining the control of output voltage and output frequency actively. The utilization of the FCS-MPC ensures that an intricate coupling between the input control and output control of the IBMC is avoided and thus allowing a natural inclusion of VSG into the control system. Lastly, the proposed scheme generates approximately the same amount of current THD even without damping resistor to the existing PWM-based method with a damping resistor, owing to the inclusion of several control targets, variables, and constraints into a single cost function for simultaneous control.

The effectiveness of the proposed control is also verified in a scale-down experiment, which highlights the grid-forming ability, the inertial behavior, and the active damping feature.

The presented work is an initial step to apply a VSG control in an AC/AC converter without a bulky energy storage element, and for future steps of this work, conducting experimental tests for a higher rating of IBMC are considered for evaluating and validating the proposed control strategy. Furthermore, supplying other loads, such as nonlinear and constant power loads to the proposed system, is also considered.

REFERENCES

[1] E. J. Bueno, S. Cobreces, F. J. Rodriguez, A. Hernandez, and F. Espinosa, "Design of a back-to-back NPC converter interface for wind turbines with squirrel-cage induction generator," *IEEE Trans. Energy Convers.*, vol. 23, no. 3, pp. 932–945, Sep. 2008.

[2] H. Bevrani, B. Francois, and T. Ise, *Microgrid Dynamics and Control*. Hoboken, NJ, USA: Wiley, 2017, pp. 6–9 and 376–393.
[3] T. Friedli, J. W. Kolar, J. Rodriguez, and P. W. Wheeler, "Comparative evaluation of three-phase AC–AC matrix converter and voltage DC-link back-to-back converter systems," *IEEE Trans. Ind. Electron.*, vol. 59, no. 12, pp. 4487–4510, Dec. 2012.
[4] P. W. Wheeler, J. Rodriguez, J. C. Clare, L. Empringham, and A. Weinstein, "Matrix converters: A technology review," *IEEE Trans. Ind. Electron.*, vol. 49, no. 2, pp. 276–288, Apr. 2002.
[5] Y.-D. Yoon and S.-K. Sul, "Carrier-based modulation technique for matrix converter," *IEEE Trans. Power Electron.*, vol. 21, no. 6, pp. 1691–1703, Nov. 2006.
[6] S. Lopez Arevalo, P. Zanchetta, P. W. Wheeler, A. Trentin, and L. Empringham, "Control and implementation of a matrix-converter-based AC ground power-supply unit for aircraft servicing," *IEEE Trans. Ind. Electron.*, vol. 57, no. 6, pp. 2076–2084, Jun. 2010.
[7] C. Klumpner, F. Blaabjerg, I. Boldea, and P. Nielsen, "New modulation method for matrix converters," *IEEE Trans. Ind. Appl.*, vol. 42, no. 3, pp. 797–806, May 2006.
[8] A. Escobar-Mejia, J. K. Hayes, J. C. Balda, and C. A. Busada, "New control strategy for indirect matrix converters operating in boost mode," in *Proc. IEEE Energy Convers. Congr. Exposit.*, Denver, CO, USA, Sep. 2013, pp. 2715–2720.
[9] P. C. Loh, F. Blaabjerg, F. Gao, A. Baby, and D. A. C. Tan, "Pulsewidth modulation of neutral-point-clamped indirect matrix converter," *IEEE Trans. Ind. Appl.*, vol. 44, no. 6, pp. 1805–1814, Nov. 2008.
[10] P. C. Loh, R. Rong, F. Blaabjerg, and P. Wang, "Digital carrier modulation and sampling issues of matrix converters," *IEEE Trans. Power Electron.*, vol. 24, no. 7, pp. 1690–1700, Jul. 2009.
[11] J. W. Kolar, M. Baumann, F. Schafmeister, and H. Ertl, "Novel three-phase AC-DC-AC sparse matrix converter," in *Proc. 17th Annu. IEEE Appl. Power Electron. Conf. Expo.*, Dallas, TX, USA, vol. 2, Mar. 2002, pp. 777–787.
[12] M. Baumann, F. Stogerer, and J. W. Kolar, "Novel three-phase AC-DC-AC sparse matrix converter," in *Proc. 17th Annu. IEEE Appl. Power Electron. Conf. Expo.*, Dallas, TX, USA, vol. 2, Mar. 2002, pp. 788–791.
[13] J. W. Kolar, F. Schafmeister, S. D. Round, and H. Ertl, "Novel three-phase AC–AC sparse matrix converters," *IEEE Trans. Power Electron.*, vol. 22, no. 5, pp. 1649–1661, Sep. 2007.
[14] G. T. Chiang and J.-I. Itoh, "Comparison of two overmodulation strategies in an indirect matrix converter," *IEEE Trans. Ind. Electron.*, vol. 60, no. 1, pp. 43–53, Jan. 2013.
[15] B. Ge, Q. Lei, W. Qian, and F. Z. Peng, "A family of Z-source matrix converters," *IEEE Trans. Ind. Electron.*, vol. 59, no. 1, pp. 35–46, Jan. 2012.
[16] T. Wijekoon, C. Klumpner, P. Zanchetta, and P. W. Wheeler, "Implementation of a hybrid AC–AC direct power converter with unity voltage transfer," *IEEE Trans. Power Electron.*, vol. 23, no. 4, pp. 1918–1926, Jul. 2008.
[17] X. Liu, P. Wang, P. C. Loh, and F. Blaabjerg, "Distributed generation interface using indirect matrix converter in boost mode with controllable grid side reactive power," in *Proc. 10th Int. Power Energy Conf. (IPEC)*, Ho Chi Minh City, Vietnam, Nov. 2012, pp. 59–64.
[18] X. Liu, P. C. Loh, P. Wang, F. Blaabjerg, Y. Tang, and E. A. Al-Ammar, "Distributed generation using indirect matrix converter in reverse power mode," *IEEE Trans. Power Electron.*, vol. 28, no. 3, pp. 1072–1082, Mar. 2013.
[19] J. Driesen and K. Visscher, "Virtual synchronous generators," in *Proc. 21st Century IEEE Power Energy Soc. Gen. Meeting-Convers. Del. Elect. Energy*, Jul. 2008, pp. 1–3.
[20] Q.-C. Zhong and G. Weiss, "Synchronverters: Inverters that mimic synchronous generators," *IEEE Trans. Ind. Electron.*, vol. 58, no. 4, pp. 1259–1267, Apr. 2011.
[21] K. Sakimoto, Y. Miura, and T. Ise, "Stabilization of a power system including inverter type distributed generators by the virtual synchronous generator," *IEEJ Trans. Power Energy*, vol. 132, no. 4, pp. 341–349, Apr. 2012.
[22] S. D'Arco and J. A. Suul, "Virtual synchronous machines—Classification of implementations and analysis of equivalence to droop controllers for microgrids," in *Proc. IEEE Grenoble Conf.*, Grenoble, France, 2013, pp. 1–7.
[23] Q.-C. Zhong, P.-L. Nguyen, Z. Ma, and W. Sheng, "Self-synchronized synchronverters: Inverters without a dedicated synchronization unit," *IEEE Trans. Power Electron.*, vol. 29, no. 2, pp. 617–630, Feb. 2014.
[24] M. Guan, W. Pan, J. Zhang, Q. Hao, J. Cheng, and X. Zheng, "Synchronous generator emulation control strategy for voltage source converter (VSC) stations," *IEEE Trans. Power Syst.*, vol. 30, no. 6, pp. 3093–3101, Nov. 2015.
[25] H. Wu, X. Ruan, D. Yang, X. Chen, W. Zhao, Z. Lv, and Q.-C. Zhong, "Small-signal modeling and parameters design for virtual synchronous generators," *IEEE Trans. Ind. Electron.*, vol. 63, no. 7, pp. 4292–4303, Jul. 2016.
[26] J. Liu, Y. Miura, and T. Ise, "Comparison of dynamic characteristics between virtual synchronous generator and droop control in inverter-based distributed generators," *IEEE Trans. Power Electron.*, vol. 31, no. 5, pp. 3600–3611, May 2016.
[27] J. Liu, Y. Miura, H. Bevrani, and T. Ise, "Enhanced virtual synchronous generator control for parallel inverters in microgrids," *IEEE Trans. Smart Grid*, vol. 8, no. 5, pp. 2268–2277, Sep. 2017.
[28] J. Lei, B. Zhou, X. Qin, J. Wei, and J. Bian, "Active damping control strategy of matrix converter via modifying input reference currents," *IEEE Trans. Power Electron.*, vol. 30, no. 9, pp. 5260–5271, Sep. 2015.
[29] J. Lei, B. Zhou, J. Bian, J. Wei, Y. Zhu, J. Yu, and Y. Yang, "Feedback control strategy to eliminate the input current harmonics of matrix converter under unbalanced input voltages," *IEEE Trans. Power Electron.*, vol. 32, no. 1, pp. 878–888, Jan. 2017.
[30] J. Rodriguez, M. P. Kazmierkowski, J. R. Espinoza, P. Zanchetta, H. Abu-Rub, H. A. Young, and C. A. Rojas, "State of the art of finite control set model predictive control in power electronics," *IEEE Trans. Ind. Informat.*, vol. 9, no. 2, pp. 1003–1016, May 2013.
[31] H. Miranda, R. Teodorescu, P. Rodriguez, and L. Helle, "Model predictive current control for high-power grid-connected converters with output LCL filter," in *Proc. 35th Annu. Conf. IEEE Ind. Electron.*, Nov. 2009, pp. 633–638.
[32] B. Arif, L. Tarisciotti, P. Zanchetta, J. C. Clare, and M. Degano, "Grid parameter estimation using model predictive direct power control," *IEEE Trans. Ind. Appl.*, vol. 51, no. 6, pp. 4614–4622, Nov./Dec. 2015.
[33] J. Hu, J. Zhu, and D. G. Dorrell, "Model predictive control of inverters for both Islanded and grid-connected operations in renewable power generations," *IET Renew. Power Gener.*, vol. 8, no. 3, pp. 240–248, Apr. 2014.
[34] L. A. Serpa, S. Ponnaluri, P. M. Barbosa, and J. W. Kolar, "A modified direct power control strategy allowing the connection of three-phase inverters to the grid through *LCL* filters," *IEEE Trans. Ind. Appl.*, vol. 43, no. 5, pp. 1388–1400, Sep./Oct. 2007.
[35] F. Donoso, A. Mora, R. Cardenas, A. Angulo, D. Saez, and M. Rivera, "Finite-set model-predictive control strategies for a 3L-NPC inverter operating with fixed switching frequency," *IEEE Trans. Ind. Electron.*, vol. 65, no. 5, pp. 3954–3965, May 2018.
[36] J. Jongudomkarn, J. Liu, and T. Ise, "Virtual synchronous generator control with reliable fault ride-through ability: A solution based on finite-set model predictive control," *IEEE J. Emerg. Sel. Topics Power Electron.*, Sep. 23, 2019, early access, doi: 10.1109/JESTPE.2019.2942943.
[37] P. Falkowski and A. Sikorski, "Dead-time compensation in a new FCS-MPC of an AC/DC converter with a LCL filter," in *Proc. 13th Sel. Issues Electr. Eng. Electron. (WZEE)*, May 2016, pp. 1–6.
[38] N. Panten, N. Hoffmann, and F. W. Fuchs, "Finite control set model predictive current control for grid-connected voltage-source converters with LCL filters: A study based on different state feedbacks," *IEEE Trans. Power Electron.*, vol. 31, no. 7, pp. 5189–5200, Jul. 2016.
[39] P. Falkowski and A. Sikorski, "Finite control set model predictive control for grid-connected AC–DC converters with LCL filter," *IEEE Trans. Ind. Electron.*, vol. 65, no. 4, pp. 2844–2852, Apr. 2018.
[40] P. Correa, J. Rodriguez, M. Rivera, J. R. Espinoza, and J. W. Kolar, "Predictive control of an indirect matrix converter," *IEEE Trans. Ind. Electron.*, vol. 56, no. 6, pp. 1847–1853, Jun. 2009.
[41] M. Rivera, J. Rodriguez, B. Wu, J. R. Espinoza, and C. A. Rojas, "Current control for an indirect matrix converter with filter resonance mitigation," *IEEE Trans. Ind. Electron.*, vol. 59, no. 1, pp. 71–79, Jan. 2012.
[42] J. Lei, B. Zhou, J. Wei, J. Bian, Y. Zhu, J. Yu, and Y. Yang, "Predictive power control of matrix converter with active damping function," *IEEE Trans. Ind. Electron.*, vol. 63, no. 7, pp. 4550–4559, Jul. 2016.
[43] Y. Zhang, W. Xie, Z. Li, and Y. Zhang, "Model predictive direct power control of a PWM rectifier with duty cycle optimization," *IEEE Trans. Power Electron.*, vol. 28, no. 11, pp. 5343–5351, Nov. 2013.
[44] P. Cortes, S. Kouro, B. La Rocca, R. Vargas, J. Rodriguez, J. I. Leon, S. Vazquez, and L. G. Franquelo, "Guidelines for weighting factors design in model predictive control of power converters and drives," in *Proc. IEEE Int. Conf. Ind. Technol.*, Feb. 2009, pp. 1–7.

[45] P. Zanchetta, "Heuristic multi-objective optimization for cost function weights selection in finite states model predictive control," in *Proc. Workshop Predictive Control Electr. Drives Power Electron.*, Oct. 2011, pp. 70–75.
[46] F. Villarroel, J. R. Espinoza, C. A. Rojas, J. Rodriguez, M. Rivera, and D. Sbarbaro, "Multiobjective switching state selector for finite-states model predictive control based on fuzzy decision making in a matrix converter," *IEEE Trans. Ind. Electron.*, vol. 60, no. 2, pp. 589–599, Feb. 2013.
[47] S. A. Davari, D. A. Khaburi, and R. Kennel, "An improved FCS-MPC algorithm for an induction motor with an imposed optimized weighting factor," *IEEE Trans. Power Electron.*, vol. 27, no. 3, pp. 1540–1551, Mar. 2012.
[48] H. Bevrani, M. Watanabe, and Y. Mitani, *Power System Monitoring and Controls*. Hoboken, NJ, USA: Wiley, 2014, pp. 187–192.
[49] S. Golestan and J. M. Guerrero, "Conventional synchronous reference frame phase-locked loop is an adaptive complex filter," *IEEE Trans. Ind. Electron.*, vol. 62, no. 3, pp. 1679–1682, Mar. 2015.
[50] J. Liu, Y. Miura, and T. Ise, "Fixed-parameter damping methods of virtual synchronous generator control using state feedback," *IEEE Access*, vol. 7, pp. 99177–99190, 2019.

JONGGRIST JONGUDOMKARN received the B.Eng. and Dipl.-Ing degrees in electrical engineering and information technology from the Technical University of Munich, Germany, in 2012 and 2013, respectively. He is currently pursuing the Ph.D. degree in electrical engineering with Osaka University, Japan. He was with the Faculty of Engineering, Khon Kaen University, Thailand, from 2014 to 2016. His research interests include distributed generators, power quality, electric machine drives, and power conversion.

JIA LIU (Member, IEEE) received the B.Eng. and M.Eng. degrees from Xi'an Jiaotong University, Xi'an, China, in 2008 and 2011, respectively, the Dipl.Ing. degree from the University of Technology of Troyes, Troyes, France, in 2011, and the Ph.D. degree in engineering from Osaka University, Osaka, Japan, in 2016. He was with Delta Electronics (Jiangsu) Ltd., Nanjing, China, from 2011 to 2012. Since 2016, he has been with the Division of Electrical, Electronic, and Information Engineering, Graduate School of Engineering, Osaka University, where he is currently an Assistant Professor. His research interests include distributed generators, microgrids, power quality, and motor drives.

YUTA YANAGISAWA (Student Member, IEEE) received the B.S. degree in electrical, electronics, and information engineering from the National Institute of Technology, Nara College (NITNC), in 2015, and the M.S. degree in electrical, electronics, and information engineering from Osaka University, in 2017, where he is currently pursuing the Ph.D. degree in electrical, electronics, and information engineering. His current research interest includes a high-frequency power conversion system with WBG semiconductors. He is a Student Member of the Institute of Electrical Engineers of Japan.

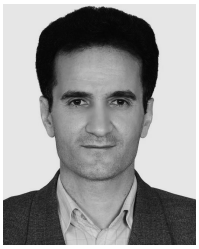

HASSAN BEVRANI (Senior Member, IEEE) received the Ph.D. degree in electrical engineering from Osaka University, Japan, in 2004.

He is currently a Full Professor and the Program Leader of the Smart/Micro Grids Research Center (SMGRC), University of Kurdistan (UOK). Over the years, he has worked as a Senior Research Fellow and a Visiting Professor with Osaka University, Kumamoto University, Japan, the Queensland University of Technology, Australia, the Kyushu Institute of Technology, Japan, Centrale Lille, France, and the Technical University of Berlin, Germany. He is the author of six international books, 15 book chapters, and more than 300 journal/conference papers. His current research interests include smart grid operation and control, power systems stability and optimization, microgrid dynamics and control, and intelligent/robust control applications in power electric industry.

TOSHIFUMI ISE (Member, IEEE) received the B.E., M.E., and D.Eng. degrees in electrical engineering from Osaka University, Osaka, Japan, in 1980, 1982, and 1986, respectively. From 1986 to 1990, he was with the Nara National College of Technology, Nara, Japan. Since 1990, he has been with the Faculty of Engineering, Graduate School of Engineering, Osaka University, and was a Professor, from August 2002 to March 2018. He is currently an Emeritus Professor with Osaka University and the President of NARA–GAKUEN Incorporated Educational Institution. His research interests include power electronics and applied superconductivity for power systems. He is a Fellow of the Institute of Electrical Engineers of Japan (IEEJ).